JOURNAL OF AIRCRAFT
Vol. 56, No. 1, January–February 2019

Dynamics and Stability of Variable-Length, Vertically-Traveling, Heavy Cables: Application to Tethered Aerostats

Dipayan Mukherjee,* Ishan Sharma,† and Shakti S. Gupta‡
Indian Institute of Technology Kanpur, Kanpur 208 016, Uttar Pradesh, India

DOI: 10.2514/1.C034931

The dynamics and stability of variable-length vertically traveling, heavy cables with an end load are investigated. Such cables act as tethers in aerostat systems. The cable is modeled as a heavy string undergoing small, planar vibrations while attached to a rigid, spherical aerostat. Aerodynamic and buoyancy forces act only on the aerostat. An asymptotic analysis for slow deployment rates provides excellent leading-order approximation to the dynamics, which is also obtained from finite element simulations. Stability of the aerostat system is then investigated computationally by considering the linear stability of the system when it is perturbed from its nominal dynamical state at any given time. It is found that, when an aerostat ascends, the cable always goes unstable after a certain time through a divergence instability. In contrast, flutter instability is found in the cable during the aerostat's descent. These stability analyses help in the development of deployment charts that relate the maximum achievable elevation to deployment rate. Such deployment charts can help in parameter selection for efficient aerostat deployment. The dynamics of the aerostat in the presence of spatiotemporally varying aerodynamic forces are also studied computationally. The paper concludes with two case studies of aerostat deployment that demonstrate the utility of the current analysis.

Nomenclature

A	=	cross-sectional area of the cable, m^2
a, $\tilde{a}$	=	dimensional (ms^{-2}) and nondimensional acceleration of ascent/descent
$\bar{E}$, $\bar{E}_P$, $\bar{E}_K$	=	nondimensional total, potential, and kinetic energies associated with the system
F_b	=	buoyancy force on the aerostat, N
$\bar{F}$	=	nondimensional net buoyancy force on the aerostat
h	=	nondimensional elevation of the aerostat
L, l	=	dimensional (m) and nondimensional lengths of the cable
$\mathbf{M}(\bar{t})$, $\mathbf{G}(\bar{t})$, $\mathbf{K}(\bar{t})$	=	$n \times n$ global mass, gyroscopic, and stiffness matrices of the system
m, $\tilde{m}$	=	dimensional (kg) and nondimensional masses of the aerostat
$\mathbf{q}(\bar{t})$	=	$n \times 1$ nodal displacements of the cable
q_{end}	=	end-tip (aerostat) deflection
$\hat{\mathbf{q}}_i$	=	$n \times 1$, ith eigenvector of the system at $\bar{t}$ equal to $\hat{t}$
r	=	radius the aerostat, m
t, $\bar{t}$	=	dimensional (s) and nondimensional times
$\bar{t}^*$	=	nondimensional critical time after which the system goes unstable
v, $\tilde{v}$	=	dimensional (ms^{-1}) and nondimensional rates of ascent/descent
x	=	position of a point on the cable, m
$y(x,t)$, $\tilde{y}(\zeta,t)$	=	transverse deflections of the cable, m
ζ	=	position of a point on the aerostat in the mapped domain; x/L
$\eta(\zeta,\bar{t})$	=	nondimensional transverse deflection
λ_i	=	ith eigenvalue of the system at $\bar{t}$ equal to $\hat{t}$
ρ	=	density of the cable, kg/m^{-3}

Received 23 January 2018; revision received 19 May 2018; accepted for publication 21 May 2018; published online 12 September 2018.

*Masters Student, Department of Mechanical Engineering, Mechanics and Applied Mathematics Group; dipayan.me2010@gmail.com.
†Professor, Department of Mechanical Engineering, Mechanics and Applied Mathematics Group; ishans@iitk.ac.in (Corresponding Author).
‡Associate Professor, Department of Mechanical Engineering, Mechanics and Applied Mathematics Group; ssgupta@iitk.ac.in.

I. Introduction

AXIALLY translating continua with varying lengths gives rise to rich dynamics [1–7] and has important engineering and aerospace applications. For example, vertically traveling heavy cables that lengthen or shorten find applications as tethers of high-altitude balloons (aerostats); see, e.g., the work of Aglietti [8]. Tethered aerostat systems have been studied by Jones and Krausman [9], Lambert and Nahon [10], Kang and Lee [11], Hembree and Slegers [12], and Mi and Gottlieb [13]. In all these studies. the focus was on the deployed state when the tether's length was fixed. Furthermore, all except Mi and Gottlieb [13] took the tether as a composition of discrete elements, and they did not model it as a continuum. Although the dynamics of variable-length tethered satellite systems was investigated by Mankala and Agrawal [14,15], no points were made by the authors on the instability in such systems. In this paper, we investigate the dynamics and stability of variable-length vertically translating, heavy cables and apply it to study the dynamics and stability of ascending/descending tethered aerostats. Figure 1a shows a sketch of the aerostat system.

Initial investigations on the spaghetti problem (i.e., an oscillating cable that is shortening in length) were carried out by Carrier [1]. Subsequently, Mansfield and Simmonds [2] investigated the dynamics of a lengthening cable, issuing from an orifice, which the authors termed a reversed spaghetti problem. Pesce [16] developed a variational framework for the variable mass systems and investigated an example of the deployment of a heavy cable from a reel. The dynamics of a horizontally deploying cable attached to an end mass has been studied by Crellin et al. [17]. In all these works, the primary goal was to investigate the evolution of the spatial configuration of the tether in time, whereas no investigation on the instability has been reported. The dynamics of axially lengthening/shortening beams and cables has been studied by Zhu and Ni [18] and Terumichi et al. [5] for application to elevator systems, and by Stylianou and Tabarrok [3] and Gosselin et al. [6] in the context of extruding beams. A more involved geometrically nonlinear formulation of axially lengthening/shortening geometrically exact beams was provided by Vu-Quoc and Li [19].

Axially translating continua are susceptible to instabilities [6,20–22]. Instability in beams of periodically varying lengths has been studied by Elmaraghy and Tabarrok [23], Zajaczkowski and Lipiński [24], and Hyun and Yoo [25]. In contrast, the change in the length of the tether of an ascending/descending aerostat is monotonic. This monotonicity in

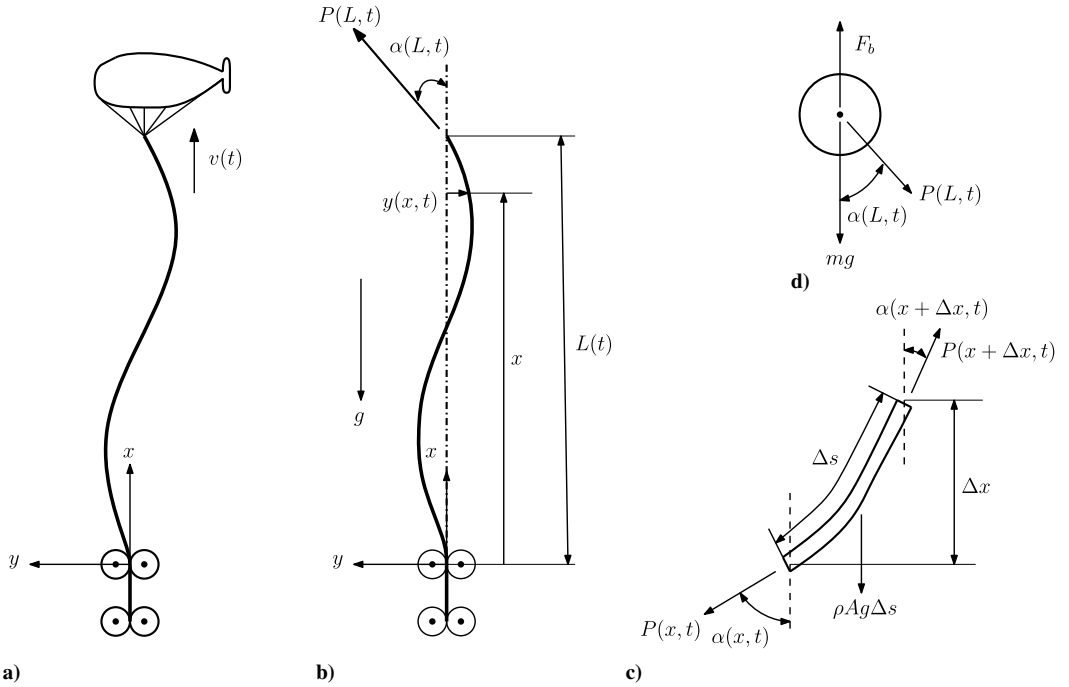

Fig. 1 Schematics of a) the aerostat system, b) the cable along with various forces acting on it, c) free body diagram of a cable element, and d) free body diagram of the aerostat, now modeled as a sphere.

the variation of the cable's length necessitates a quasi-static eigenvalue analysis of the system, as employed by Stylianou and Tabarrok [4] and Gosselin et al. [6]. Nawrotzki and Eller [26] used the quasi-static eigenvalue analysis to investigate stability of nonlinear structures. Zhu and Ni [18] studied the stability of lengthening/shortening elevator cables in light of evolution of the total mechanical energy of the system. However, it was shown by Yang and Mote [27] and Ziegler ([28] pp. 36-40) that the evolution of energy could not be a measure of the stability of a dynamical system in the presence of gyroscopic terms, which typically arise in the study of travelling cables.

Our mathematical model is as follows. We model the cable as a tensioned, heavy string of varying length and the aerostat as a rigid sphere. As a first step, we restrict ourselves to small oscillations in a plane. Aerodynamic and buoyancy effects are considered on the aerostat alone. Our aerodynamic model, based on work by Tchen [29], Corrsin and Lumley [30], and Maxey and Riley [31], includes the effects of the flow's pressure gradient, Stokes drag, and added mass, but it ignores vortex shedding. We analyze the dynamics of the aerostat system, both through an asymptotic analysis of a reduced-order model and by a finite element analysis. The stability of the aerostat system during deployment is found to depend crucially on the stability of the lengthening/shortening cable (tether). This stability is investigated computationally following the quasi-static linear stability analysis mentioned previously. We find that all ascending aerostats are susceptible to divergence instabilities, which limits the maximum elevation that can be achieved in terms of its deployment rate. Descending aerostats, on the other hand, go unstable through a flutter instability. We note that we do not incorporate structural damping in the cable at present, and this leads to a more conservative description of instability.

This paper is organized as follows. In Sec. II, we derive the equations of motion for ascending/descending aerostat systems using both linear momentum balance and variational principle. Asymptotic approximations are employed to investigate the vibrations of a slowly ascending/descending aerostat system in Sec. III. Divergence instability in ascending aerostats is then demonstrated in Sec. IV. This instability is then investigated through an eigenvalue analysis. Instability in descending aerostats is studied in Sec. V. We then investigate the forced vibration of ascending/descending aerostat systems under steady, temporally nonuniform air flow in Sec. VI. Finally, in Sec. VII, we conclude with two case studies of ascending aerostats that demonstrate how we may use our results.

II. Equations of Motion

In this section, we summarize the equations of motion for a lengthening/shortening cable, modeling it as a heavy, inextensible string of varying length; the details of the derivation are in the supplementary material and [32]. Figure 1a shows our model for the aerostat system: the aerostat is a rigid sphere of mass m that is attached to a uniform cable of uniform density ρ and cross-sectional area A. We consider the rollers at the base to be small and smooth. The length of the cable changes at a rate of $v(t) = \dot{L}(t)$, where $(\cdot)$ denotes differentiation with respect to time t. The diagram in Fig. 1b shows the body and end forces on the cable. The tension in the cable is $P(x, t)$. We present the free body diagram of a cable element of length Δs and the aerostat in Fig. 1c.

The distribution of tension in the heavy cable is obtained by integrating the vertical balance of linear momentum along the cable:

$$P(x,t) = F_c(t) - \rho A\{g + \ddot{L}(t)\}\{L(t) - x\} \tag{1}$$

where $F_c(t) = P(x,t)|_{x=L(t)}$ is the force exerted by the aerostat on the cable.

To derive equations of motion from variational principles, we first estimate kinetic and potential energies associated with the cable. Expressions for kinetic and potential energy associated with lengthening/shortening cables are respectively,

$$T = \frac{1}{2}\int_0^{L(t)} \rho A[\{y_{,t} + \dot{L}(t)y_{,x}\}^2 + \dot{L}^2(t)]\,\mathrm{d}x \tag{2}$$

and

$$V = \frac{1}{2}\int_0^{L(t)} P(x,t)(y_{,x})^2\,\mathrm{d}x \tag{3}$$

where $y(x, t)$ is the transverse deflection of the cable, and the subscripts indicate partial differentiation. The preceding expressions are the same as for a traveling cable, fixed at both its ends; see [18,33,34]. However, in this case, the length of the cable $L(t)$ is not constant and the tension $P(x, t)$ in the cable may vary with length and time. We henceforth suppress the time dependence of $L(t)$ and write it as L. We now express the action integral as

$$\int_{t_1}^{t_2} (\delta T - \delta V)\,\mathrm{d}t = 0 \tag{4}$$

where $\delta(\cdot)$ is the variational operator. We note that the spatial domain of integration is changing with time. A direct attempt to derive equations of motion from this may invite additional complexity. To overcome this problem, we perform a change of variable [19,35]. We take $\zeta = x/L$ such that $0 \le \zeta \le 1$. The transverse displacement becomes $\tilde{y}(\zeta, t) = y(x, t)$. Derivatives transform as

$$y_{,x} = \tilde{y}_{,\zeta}\frac{\partial \zeta}{\partial x} = \frac{\tilde{y}_{,\zeta}}{L}, \quad \text{and} \quad y_{,t} = \tilde{y}_{,t} + \tilde{y}_{,\zeta}\frac{\partial \zeta}{\partial t} = \tilde{y}_{,t} - \tilde{y}_{,\zeta}\frac{\zeta \dot{L}}{L}$$

The modified expressions for kinetic and potential energy are then

$$T = \frac{1}{2}\int_0^1 \rho A L\left[\left\{\tilde{y}_{,t} + (1-\zeta)\tilde{y}_{,\zeta}\frac{\dot{L}}{L}\right\}^2 + \dot{L}^2\right]\mathrm{d}\zeta \tag{5}$$

and

$$V = \frac{1}{2}\int_0^1 \left[\frac{F_c(t)}{L} - \rho A\{g + \ddot{L}(t)\}(1-\zeta)\right]\tilde{y}_{,\zeta}^2\,\mathrm{d}\zeta \tag{6}$$

where $F_c(t) = P(L, t)$ is the applied force at the free end of the cable. Substituting the preceding in Eq. (4) and integrating the result by parts, we obtain the governing equation for the aerostat system (see the supplementary material for details):

$$\rho A L\tilde{y}_{,tt} + 2\rho A(1-\zeta)\dot{L}\tilde{y}_{,\zeta t} + \rho A(1-\zeta)\ddot{L}\tilde{y}_{,\zeta} + \rho A\frac{\partial}{\partial \zeta}\left\{(1-\zeta)^2\frac{\ddot{L}^2}{L}\tilde{y}_{,\zeta}\right\}$$
$$= \frac{\partial}{\partial \zeta}\left[\left\{\frac{F_c}{L} - \rho A(g+\ddot{L})(1-\zeta)\right\}\tilde{y}_{,\zeta}\right] \tag{7}$$

and the geometric boundary condition at the roller (lower) end:

$$\tilde{y} = 0 \quad \text{at} \quad \zeta = 0 \tag{8}$$

To obtain the natural boundary condition at the upper end of the cable and the expression for the force F_c on the cable, we balance vertical and horizontal forces on the aerostat attached to the cable at $x = L$; see Fig. 1d. We obtain, respectively,

$$F_c(t) = F_b - m(g + \ddot{L}) =: F - m\ddot{L} \tag{9a}$$

and

$$m(y_{,tt} + 2y_{,xt}\dot{L} + y_{,xx}\dot{L}^2 + y_{,x}\ddot{L}) + F_c(t)y_{,x} = 0 \quad \text{at} \quad x = L \tag{9b}$$

where F_b is the buoyancy force on the aerostat. Combining these two equations and expressing in terms of $\zeta = x/L$ yields

$$m\left(\tilde{y}_{,tt} - \frac{\ddot{L}}{L}\tilde{y}_{,\zeta}\right) + \frac{F}{L}\tilde{y}_{,\zeta} = 0 \quad \text{at} \quad \zeta = 1 \tag{10}$$

which represents the natural boundary condition for the system at the upper end of $\zeta = 1$. We nondimensionalize Eq. (7) to find

$$l\eta_{,\bar{t}\bar{t}} + 2(1-\zeta)\dot{l}\eta_{,\zeta\bar{t}} + (1-\zeta)\ddot{l}\eta_{,\zeta} + \frac{\partial}{\partial \zeta}\left\{(1-\zeta)^2\frac{\dot{l}^2}{l}\eta_{,\zeta}\right\}$$
$$= \frac{\partial}{\partial \zeta}\left[\left\{\frac{1}{l} - \tilde{m}\frac{\ddot{l}}{l} - \left(\frac{1}{\tilde{F}} + \ddot{l}\right)(1-\zeta)\right\}\eta_{,\zeta}\right] \tag{11}$$

where the nondimensional deflection

$$\eta(\zeta, \bar{t}) = \tilde{y}(\zeta, t)/L_0$$

is defined in terms of initial length L_0 of the cable, and the nondimensional time is

$$\bar{t} = t\frac{1}{L_0}\sqrt{\frac{F}{\rho A}}$$

whereas the total derivative with respect to $\bar{t}$ is again denoted by $(\cdot)$, the nondimensional length of the cable is $l(\bar{t}) = L/L_0$, the nondimensional external force is $\tilde{F} = F/\rho A g L_0$, and the nondimensional mass of the aerostat is $\tilde{m} = m/\rho A L_0$. We define the nondimensional velocity $\tilde{v} = \dot{l} = \dot{L}\sqrt{\rho A/F}$, where $\sqrt{F/\rho A}$ is the speed of travelling waves in a string kept at a constant tension F. Finally, we define a nondimensional acceleration of $\tilde{a} = \ddot{l} = \ddot{L}\rho A/F$. The boundary conditions [Eqs. (8) and (10)] are nondimensionalized as

$$\eta = 0 \quad \text{at} \quad \zeta = 0 \tag{12a}$$

and

$$\tilde{m}\left(\eta_{,\bar{t}\bar{t}} - \frac{\ddot{l}}{l}\eta_{,\zeta}\right) + \frac{1}{l}\eta_{,\zeta} = 0 \quad \text{at} \quad \zeta = 1 \tag{12b}$$

The transverse vibrations of the lengthening/shortening cable are governed by the partial differential equation [Eq. (11)] along with the boundary conditions [Eq. (10)].

We make two comments. The system does not preserve energy due to a continuous supply/depletion of mass at the cable's lower end. Thus, the system is non-Hamiltonian. We also note the presence of the gyroscopic term $\eta_{,\zeta\bar{t}}$ in Eq. (11), which affects the stability of the system but does not contribute to the system's kinetic energy. Thus, an energetic stability analysis will be incomplete because it will overlook the role of such gyroscopic terms; see, e.g., the work of Ziegler ([28] pp. 36–40).

III. Slowly Lengthening/Shortening Cables

It is possible to make significant progress through the analysis of a reduced-order model when the cable's lengthening/shortening rate is small. To develop a reduced-order model of the system, we express the deflection $\eta(\zeta, \bar{t})$ as

$$\eta(\zeta, \bar{t}) = \sum_{i=0}^{n} W_i(\zeta)q_i(\bar{t})$$

where $W_i(\zeta)$ is the ith mode of vibration that satisfies the geometric boundary condition [Eq. (12a)], and $q_i(\bar{t})$ is the temporal evolution of the mode. A reduced-order model is obtained by considering only the first mode, which is taken to be

$$W(\zeta) = \sin\left(\frac{\pi}{2}\zeta\right) \tag{13}$$

We replace the preceding approximation in the weighted residual form associated with Eq. (11) and the natural boundary condition [Eq. (12b)], and we follow Galerkin's method; see the work of Hagedorn and Dasgupta ([36] pp. 47–49). Projection onto the first mode leads to a single-degree-of-freedom approximation of Eq. (11), viz.,

$$(2\tilde{m} + l)\ddot{q}(\bar{t}) + \dot{l}\,\dot{q}(\bar{t}) + \left\{\chi\ddot{l} + \kappa\left(\frac{\ddot{l}}{l} + 4\frac{\dot{l}^2}{l^2}\right) + \frac{\alpha}{l} + \beta\frac{\dot{l}^2}{l} + \gamma\right\}q(\bar{t}) = 0 \tag{14}$$

where

$$\alpha = \frac{\pi^2}{4}, \qquad \beta = -\left(\frac{1}{2} + \frac{\pi^2}{12}\right), \qquad \gamma = -\frac{1}{\tilde{F}}\left(\frac{\pi^2}{8} + \frac{1}{2}\right),$$
$$\kappa = -\frac{\pi^2}{4}\tilde{m} \quad \text{and} \quad \chi = \left(\frac{1}{2} - \frac{\pi^2}{8}\right) \tag{15}$$

We now investigate the single-degree-of-freedom model [Eq. (14)] through asymptotics.

A. Asymptotic Analysis

The time scale of transverse vibrations may be estimated from the frequency of the first mode of a cable of fixed length L, and this yields $2L/\sqrt{F/\rho A}$ ([36] pp. 47–49). This time scale, however, changes with the cable's length on a time scale L/v associated with the deployment rate v of the cable. For typical aerostat systems, the ratio of these two time scales is $v/\sqrt{F/\rho A} \ll 1$, so that fast transverse vibrations are modified slowly by the deployment rate. Indeed, for usual deployment rates of $v = 1.0$–1.2 ms^{-1} [37,38] and representative values of $F(\approx 350$ kN) and $\rho A(\approx 3.75$ kg/m$^{-1})$, we find that $v/\sqrt{F/\rho A}$ lies in the range 0.002–0.005. We thus expect the system's dynamics to display "slow" and "fast" time scales associated with, respectively, its axial lengthening/shortening and its transverse vibrations.

Given the preceding discussion, we express time as

$$\bar{t} = T + \tau + \mathcal{O}(\epsilon^2) \tag{16}$$

where $T = \mathcal{O}(\bar{t})$, $\tau = \epsilon\bar{t}$ is the slow time scale; and $0 < \epsilon \ll 1$ is a small parameter introduced to aid the perturbation analysis. By our assumption, $l(T, \tau) = l(\tau)$. It is shown in [32] that a regular multiple scale perturbation method fails for nonautonomous systems like Eq. (14). This drawback of the multiple scale method may be overcome through the Wentzel–Kramers–Brillouin (WKB) method; see ([39] pp. 556–559) or ([40] pp. 127–129). In the WKB method, we assume q to be of the form

$$q = q(T^*, \tau, \epsilon)$$

where $T^* \neq T$ is a modified fast time, defined as $T^* = \phi(\tau)/\epsilon$; the function $\phi(\tau)$ will be defined later. The choice of $\phi(\tau)$ must ensure a periodic solution of q in T^* so that $q(T^*, \tau, \epsilon) = q(2\pi + T^*, \tau, \epsilon)$. Employing the definitions of T^* and τ and treating them as independent quantities, the chain rule yields

$$\frac{\mathrm{d}(\cdot)}{\mathrm{d}\bar{t}} = \frac{\partial\phi(\tau)}{\partial\tau}\frac{\partial(\cdot)}{\partial T^*} + \epsilon\frac{\partial(\cdot)}{\partial\tau} \tag{17a}$$

and

$$\frac{\mathrm{d}^2(\cdot)}{\mathrm{d}\bar{t}^2} = \left\{\frac{\partial\phi(\tau)}{\partial\tau}\right\}^2\frac{\partial^2(\cdot)}{\partial T^{*2}} + \epsilon\left\{2\frac{\partial\phi(\tau)}{\partial\tau}\frac{\partial^2(\cdot)}{\partial T^*\partial\tau} + \frac{\partial^2\phi(\tau)}{\partial\tau^2}\frac{\partial(\cdot)}{\partial T^*}\right\} + \epsilon^2\frac{\partial^2(\cdot)}{\partial\tau^2} \tag{17b}$$

Expanding temporal derivatives in Eq. (14) as shown earlier and collecting $\mathcal{O}(1)$ terms, we obtain

$$\left\{\frac{\partial\phi(\tau)}{\partial\tau}\right\}^2\frac{\partial^2 q_0(T^*, \tau)}{\partial T^{*2}} + \psi(\tau)^2 q_0(T^*, \tau) = 0 \tag{18}$$

where

$$\psi(\tau) = \left[\frac{\alpha}{l(\tau)\{2\tilde{m} + l(\tau)\}} + \frac{\gamma}{2\tilde{m} + l(\tau)}\right]^{(1/2)}$$

We now define

$$\phi(\tau) = \int_0^\tau \psi(\tau)\,\mathrm{d}\tau$$

so that $\partial\phi(\tau)/\partial\tau = \psi(\tau)$, and this simplifies Eq. (18).

With this, the general solution of Eq. (18) is obtained as

$$q_0(T^*, \tau) = A_0(\tau)e^{iT^*} + \bar{A}_0(\tau)e^{-iT^*}$$

To obtain $A_0(\tau)$, we collect $\mathcal{O}(\epsilon)$ terms from Eq. (14) after expanding its temporal derivatives through Eq. (12) to find

$$\frac{\partial^2 q_1(T^*, \tau)}{\partial T^{*2}} + q_1(T^*, \tau) + \frac{2}{\psi(\tau)}\frac{\partial^2 q_0(T^*, \tau)}{\partial T^*\partial\tau} + \frac{1}{\psi(\tau)^2}\frac{\partial\psi(\tau)}{\partial\tau}\frac{\partial q_0(T^*, \tau)}{\partial T^*} + \frac{1}{\psi(\tau)\{2\tilde{m} + l(\tau)\}}\frac{\mathrm{d}l(\tau)}{\mathrm{d}\tau}\frac{\partial q_0(T^*, \tau)}{\partial T^*} = 0 \tag{19}$$

To obtain periodic solutions, we collect secular terms (coefficients of e^{iT^*}) in Eq. (19) and equate them to zero. This yields the equation

$$\frac{\mathrm{d}A_0(\tau)}{\mathrm{d}\tau} + \frac{1}{2\psi(\tau)}\frac{\mathrm{d}\psi(\tau)}{\mathrm{d}\tau}A_0(\tau) + \frac{1}{2(2\tilde{m} + l(\tau))}\frac{\mathrm{d}l(\tau)}{\mathrm{d}\tau}A_0(\tau) = 0 \tag{20}$$

for $A_0(\tau)$, for which the solution is

$$A_0(\tau) = \frac{a_0}{\sqrt{\psi(\tau)\{2\tilde{m} + l(\tau)\}}} = \frac{a_0}{\sqrt[4]{\{\alpha/l(\tau) + \gamma\}\{2\tilde{m} + l(\tau)\}}} \tag{21}$$

where the constant a_0 is fixed by initial conditions. The preceding represents the evolution of the amplitude as a function of slow time τ. Finally, the leading-order solution is

$$q_0(\bar{t}) = q_0(T^*, \tau, \epsilon) = A_0(\tau)\cos T^* = A_0(\tau)\cos\left\{\frac{\phi(\tau)}{\epsilon}\right\} \tag{22}$$

Substituting $\phi(\tau)$ in the preceding equation yields

$$q_0(T, \tau) = A_0(\tau)\cos\left[\left\{\frac{1}{\tau}\int_0^\tau \psi(\tau)\,\mathrm{d}\tau\right\}T\right] = A_0(\tau)\cos\{\bar{\psi}(\tau)T\} \tag{23}$$

where

$$\bar{\psi}(\tau) = \frac{1}{\tau}\int_0^\tau \psi(\tau)\,\mathrm{d}\tau$$

is the leading-order estimate of the first natural frequency. In Eq. (23), the slowly varying amplitude $A_0(\tau)$ forms the envelope of the fast oscillations represented by the cosine term.

We now approximate the energy associated with the assumed mode [Eq. (13)].

B. Energy Associated with the First Mode

The total energy of axially lengthening/shortening cables does not remain constant in time because we are constantly adding/subtracting mass from the system. Thus, we expect the energy associated with the first mode [Eq. (13)] to vary with time.

The leading-order approximation of the total nondimensional energy associated with the first mode [Eq. (13)] is

$$\tilde{E}(\tau) = \frac{1}{4}\left\{\frac{\alpha}{l(\tau)} + \gamma g\right\}A_0^2(\tau) + \mathcal{O}(\epsilon) \tag{24}$$

where the nondimensional energy is $\tilde{E} = E/FL_0$, the constants α and γ are given by Eq. (15), and A_0 is obtained from Eq. (22). Equation (24) is derived in the supplementary material and from [32]. We now compare our approximations $A_0(\tau)$, $\bar{\psi}(\tau)$, and $\tilde{E}(\tau)$ with direct numerical solutions.

C. Comparison with Full Finite Element Solution

We now compare our reduced-order analysis with solutions found using a finite element (FE) analysis for which the details are available in the Appendix. In our FE and reduced-order analysis, we use the design parameters employed for the aerostat system, which were studied by Aglietti et al. [41] and Aglietti [8]. The parameters are shown in Table 1. We will consider the temporal evolutions of the envelope of the amplitude $A_0(\tau)$ and the natural frequency $\bar{\psi}(\tau)$ corresponding to the first approximated mode and the energy $E(\tau)$ associated with this mode.

Table 1 Design parameters for the aerostat system

Parameter	Value
Tether mass per unit length ρA	3.750 kg/m^{-1}
Aerostat mass + payload m	15,000 kg
Buoyancy force F_b	500 kN
Aerostat radius r	30 m

We begin with the envelope $A_0(\tau)$ of oscillation. We investigate two examples here. First, we consider a cable that lengthens and shortens at a constant rate of $\tilde{v} = 5 \times 10^{-4}$; the results are shown in Figs. 2a and 2b, respectively. Next, in Figs. 2c and 2d, we consider, respectively, a cable that lengthens and shortens from rest at a constant acceleration of $\tilde{a} = 5 \times 10^{-7}$. Our results qualitatively match those of Zhu and Ni [18], whose boundary conditions were, however, different.

Evolutions of the first natural frequency obtained from FE computation [corresponding to the first mode of Eq. (A5)] and from the asymptotic analysis of the reduced-order model are presented in Fig. 3. We note that the change in frequency of the single-mode approximation [Eq. (23)] matches the FE solution qualitatively. The deviations are because the first mode shape of the system, as obtained from FE computations, is not the same as our assumed mode shape [Eq. (13)]; cf. Fig. 4.

We present the evolution of energy associated with the first eigenmode obtained from FE computations for various lengthening/shortening rates in Fig. 5. Initially, the cable is deformed into the shape of the first eigenmode of a cable with a constant length of $l = 1$, which is the initial length of the lengthening/shortening cable. The initial configuration of the cable is shown with a dashed line in Fig. 4. We also show the evolution of energy $E(\tau)$ obtained from the asymptotic analysis in the same figure. Our approximation for energy $E(\tau)$ again matches qualitatively with the energy associated with the first eigenmode of Eq. (A5). The departure from an exact match may be explained as in the case of natural frequency.

We see in Fig. 5 that the total energy of oscillations decreases for a lengthening cable and grows to infinity as the length tends to zero for a shortening cable. A stability analysis of axially lengthening and shortening cables, based on the evolution of total energy in time, was presented by Zhu and Ni [18]. These authors assume that the system is unstable if the total energy associated with the perturbed cable increases with time. Thus, axially shortening cables are claimed to be inherently unstable. However, there is no obvious reason for an energetic stability criterion to indicate Lyapunov stability in the current non-Hamiltonian system that has gyroscopic terms; see, e.g., the works of Yang and Mote [27] and Ziegler ([28] pp. 36–40). Therefore, in the next section, we will investigate stability through a spectral analysis.

IV. Instability in Ascending Aerostats

In the previous section, we discussed the dynamics of a heavy cable, for which its rate of lengthening/shortening is slow. We now consider the dynamics of the aerostat system for faster rates of ascent. Our FE computations, using parameters given in Table 1, show that, at a constant rate of ascent $\tilde{v} = 0.0175$, displacements of the lower nodes start increasing rapidly after $\bar{t} > 9.7 \times 10^5$; see Figs. 6a and 6b. Additionally, for $\bar{t} > \times 10^5$, the nodal displacements no longer remain oscillatory. Figures 6c and 6d show that, as time elapses, the upper

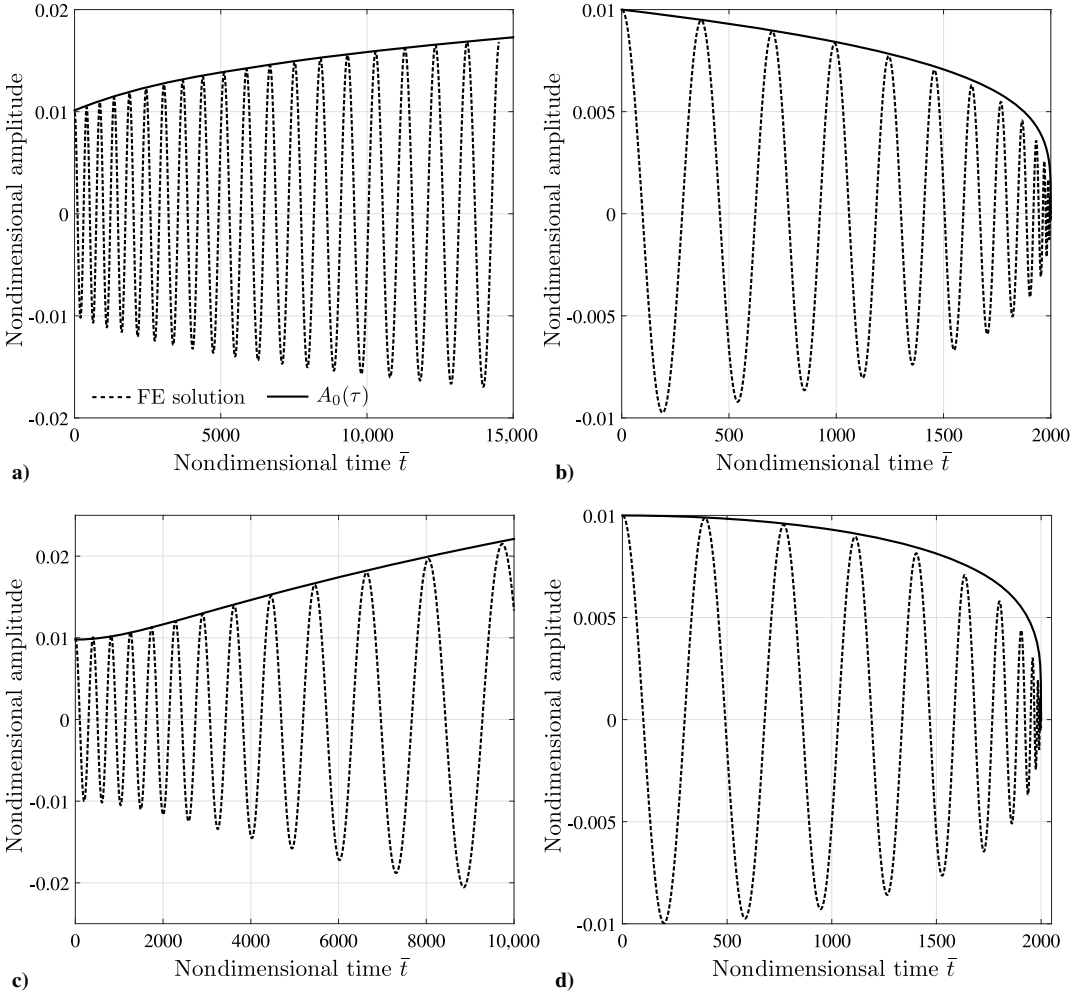

Fig. 2 Time series response, FE solution with $A_0(\tau)$: a) lengthening and b) shortening cable with constant rate of $\tilde{v} = 5 \times 10^{-4}$, and c) lengthening and d) shortening cable with constant acceleration of $\tilde{a} = 5 \times 10^{-7}$.

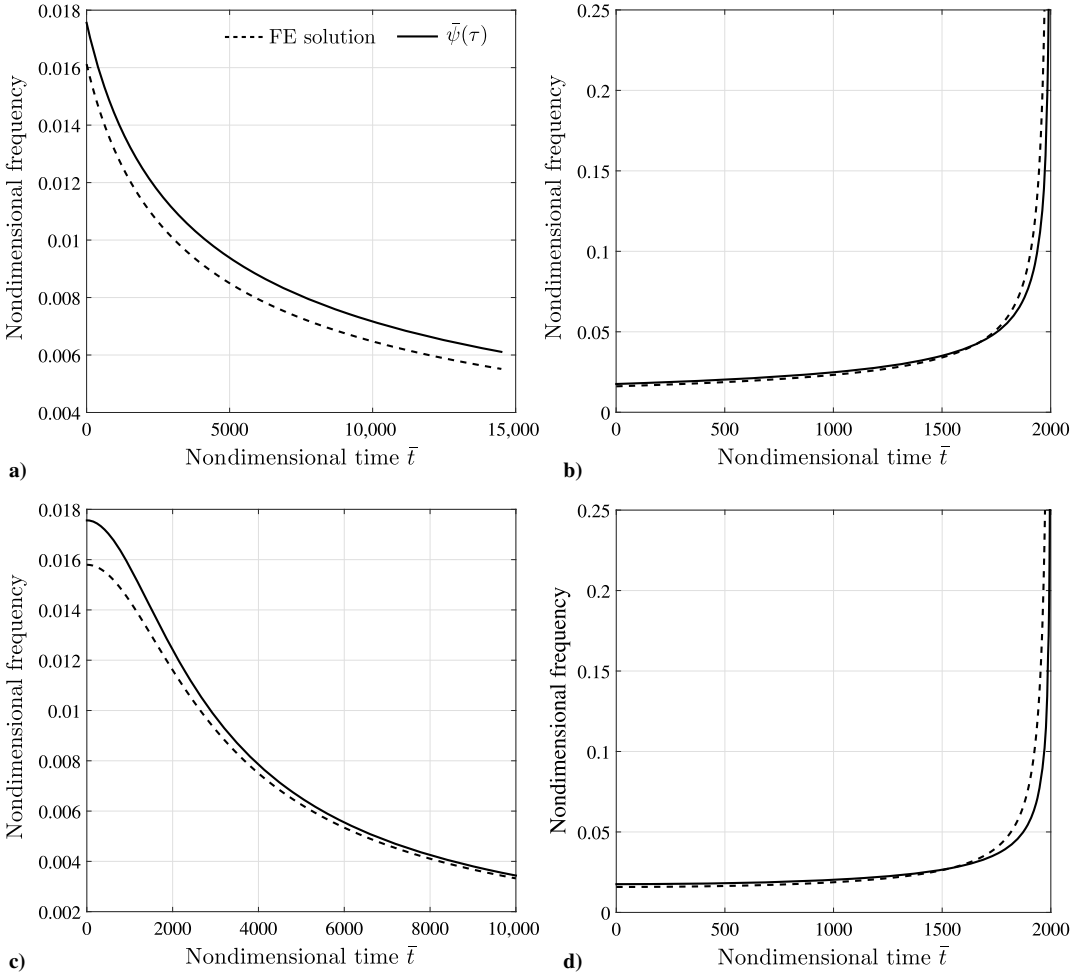

Fig. 3 Evolution of the first natural frequency, FE solution with $\bar{\psi}(\tau)$: a) lengthening and b) shortening cable with constant rate of $\tilde{v} = 5 \times 10^{-4}$, and c) lengthening and d) shortening cable with a constant acceleration of $\tilde{a} = 5 \times 10^{-7}$.

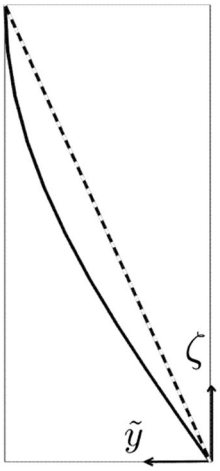

Fig. 4 Comparison of the shape of the first eigenmode of a cable in the $\zeta = x/L$ domain obtained from FE computations (dashed line) with the single-mode approximation [Eq. (13)] (solid line).

nodes gradually begin rapid and aperiodic motion. We will subsequently identify this rapid increase of nodal deflections as instability of ascending cables. Note that the jaggedness at the bottom of the cable is random, and it increases with the number of finite elements. This is because the poststability behavior of the cable cannot be captured by the model, and thus the individual nodal displacements randomly approach infinity as the instability sets in.

Figure 6 shows that instability first sets in at the lowest free computational node (node 2) of the cable and then propagates upward. Thus, we plot the deflection $q_2(\bar{t})$ of node 2 against $\bar{t}$ to investigate how the ascending rate $\tilde{v}$ affects the critical time $\bar{t} = \bar{t}^*$; after which, the cable becomes unstable.

The variation of q_2 with $\bar{t}$ for different constant rates $\tilde{v}$ is shown in Fig. 7. We see that, after a certain $\bar{t} = \bar{t}^*$, q_2 ceases to oscillate about a mean. Instead, q_2 increases rapidly for $\bar{t} \geq \bar{t}^*$, thereby destabilizing the system. Figure 7 also shows that $\bar{t}^*$ reduces with increasing $\tilde{v}$. Additionally, we observe that, at the onset of instability, the total energy associated with the aerostat system $\bar{E}$ becomes negative and rapidly approaches $-\infty$ as $\bar{t} > \bar{t}^*$; see insets in Fig. 7. To understand why $\bar{E} \to -\infty$ for $\bar{t} > \bar{t}^*$, we write the total energy as

$$\bar{E} = \frac{1}{2}\dot{q}^T \mathbf{M} \dot{q} + \frac{1}{2} q^T \mathbf{K} q \tag{25}$$

where $\mathbf{M}$ and $\mathbf{K}$ are the global mass and stiffness matrices, respectively; and q and $\dot{q}$ are the nodal displacement and velocity column vectors, respectively. See the Appendix for details. The first term in the preceding equation represents the kinetic energy $\bar{E}_K$, whereas the second term is the potential energy $\bar{E}_P$ of the system. Now, for $\bar{E}$ to be negative, either $\bar{E}_K$, $\bar{E}_P$, or both must be negative. From the Appendix, we find that $\mathbf{M}$ is a diagonal matrix consisting of strictly nonnegative and real elements. Thus, $\mathbf{M}$ is positive definite for all $\bar{t}$ and $\bar{E}_K$ cannot be negative for any $\dot{q}$. Thus, it must be that $\bar{E}_P$ becomes negative for $\bar{t} \geq \bar{t}^*$, which in turn implies that $\mathbf{K}$ no longer remains positive definite after $\bar{t} \geq \bar{t}^*$.

These observations are now validated by FE computations in Fig. 8, which reports the variations of $\bar{E}$, $\bar{E}_K$, and $\bar{E}_P$ with $\bar{t}$. Figure 8 shows that $\bar{E}_P$ becomes negative before $\bar{E}$ does, and it eventually forces $\bar{E}$ to become negative. We note that $\bar{E}_K$ remains positive for all

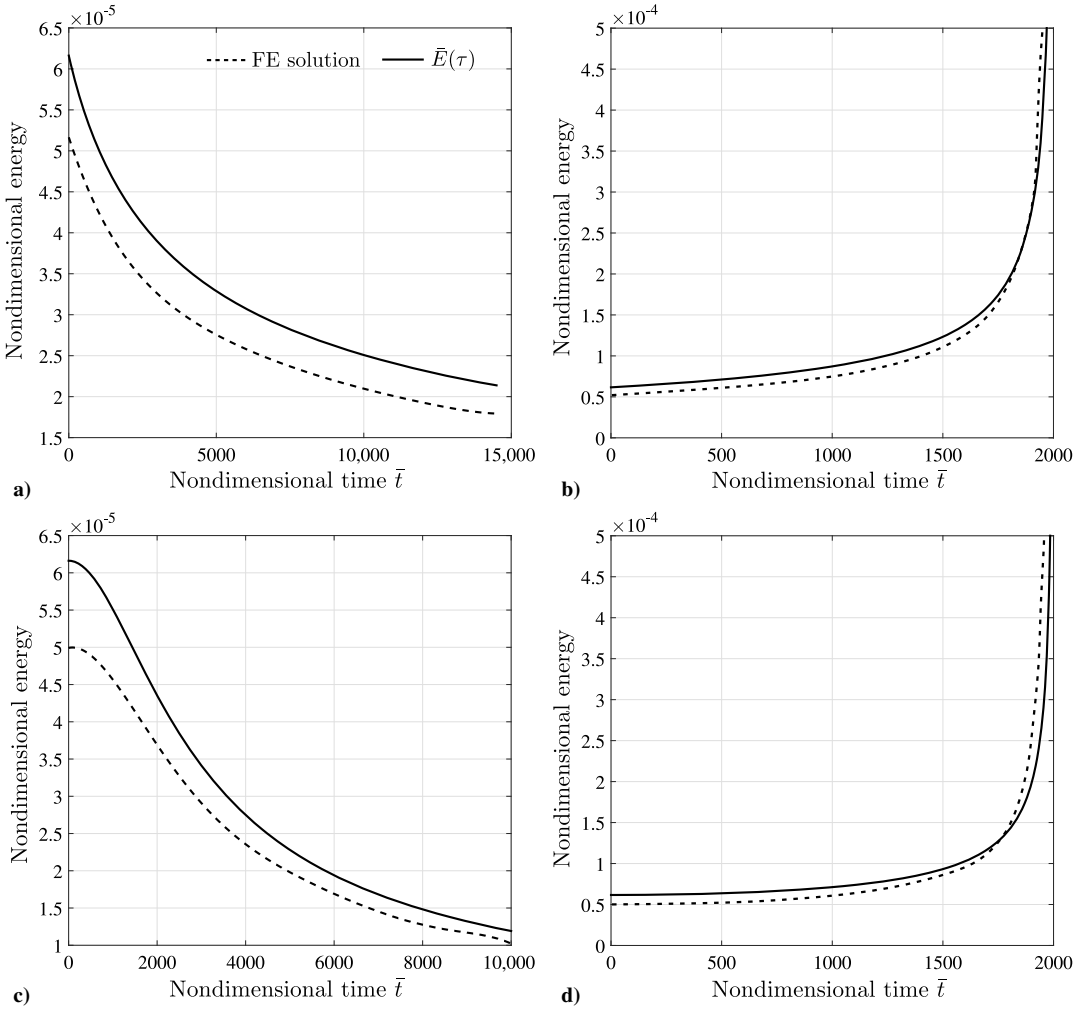

Fig. 5 Energy associated with the first eigenmode, FE solution with $\bar{E}(\tau)$: a) lengthening and b) shortening with constant rate of $\tilde{v} = 5 \times 10^{-4}$, and c) lengthening and d) shortening with constant acceleration of $\tilde{a} = 5 \times 10^{-7}$.

$\bar{t}$, confirming the positive definiteness of $\mathbf{M}$ for all $\bar{t}$. The sudden increase in $\bar{E}_K$ for $\bar{t} > \bar{t}^*$ is due to the rapid increase of nodal velocities $\dot{\tilde{u}}$ after the onset instability. The increasingly steep nature of $q_2(\bar{t})$ for $\bar{t} > \bar{t}^*$, shown in Fig. 7, confirms this rapid growth in nodal velocities.

We now investigate the effect of positive definiteness of K on stability of the system by considering the eigenvalues of

$$\mathbf{M}(\bar{t})\ddot{q}(\bar{t}) + \mathbf{G}(\bar{t})\dot{q}(\bar{t}) + \mathbf{K}(\bar{t})q(\bar{t}) = 0 \tag{26}$$

where $\mathbf{G}(\bar{t})$ is the gyroscopic matrix defined in the Appendix; see also the work of Yang and Mote [27] and Ziegler ([28] pp. 36–40). We find that $\det\{\mathbf{G}(\bar{t})\}$ is constant in $\bar{t}$ for a fixed $\tilde{v}$, whereas the determinants of the mass matrix ($\det\{\mathbf{M}(\bar{t})\}$) and the stiffness matrix ($\det\{\mathbf{K}(\bar{t})\}$) are, respectively, monotonically increasing and monotonically decreasing with $\bar{t}$. In contrast to the stability analysis of structures with periodically varying lengths [23–25], we investigate the stability at any time $\bar{t} = \hat{t}$ of the aerostat system through the linearized dynamics of the perturbed system that, in the unperturbed state, is taken to be of fixed length: $l^* = l(\hat{t})$. This quasi-static stability analysis gives a good approximation of the stability limits for continuous systems with monotonically increasing/decreasing lengths [4,6,26]. Indeed, as we will see later in this section, quasi-static instability predictions match well with direct numerical simulations.

At a given instant of time $\bar{t} = \hat{t}$, we decompose $q(\hat{t})$ into a linear combination of the eigenmodes of Eq. (26):

$$q(\hat{t}) = \sum_{i=1}^{n} \exp(\lambda_i \hat{t})\hat{q}_i$$

where λ_i is the ith eigenvalue of the system [Eq. (26)] at $\bar{t} = \hat{t}$, and $\hat{q}_i$ is the corresponding eigenvector. We represent the eigenvalue problem associated with Eq. (26) as the matrix equation

$$\lambda_i^2 \mathbf{M}(\hat{t})\hat{q}_i + \lambda_i \mathbf{G}(\hat{t})\hat{q}_i + \mathbf{K}(\hat{t})\hat{q}_i = 0$$

Premultiplying the preceding equation with $\hat{q}_i^*$, which is the conjugate transpose of $\hat{q}_i$, we obtain the scalar equation

$$A(\hat{t})\lambda_i^2 + B(\hat{t})\lambda_i + C(\hat{t}) = 0$$

where $A = \hat{q}_i^* \mathbf{M}(\hat{t})\hat{q}_i$, $B = \hat{q}_i^* \mathbf{G}(\hat{t})\hat{q}_i$, and $C = \hat{q}_i^* \mathbf{K}(\hat{t})\hat{q}_i$ are functions of time. Now, λ_i is obtained as

$$\lambda_i = \frac{1}{2}(-g \pm \sqrt{g^2 - 4k}) \tag{27}$$

where $g = B/A$, and $k = C/A$. The system is defined to be linearly unstable if at least one $\lambda_i = \alpha_i + \imath\beta_i$, with $\imath = \sqrt{-1}$, has $\alpha_i = \beta_i = 0$ or $\alpha_i \geq 0$ and $\beta_i \neq 0$ ([42] pp. 28–33, [28] pp. 36–40). From Eq. (27), we observe that one root vanishes when $k = 0$ [i.e., when $\det(\mathbf{K}) = 0$] and divergence instability sets in when k becomes negative. Thus, as in undamped gyroscopic systems [27,43], any negative definite $\mathbf{K}$ implies divergence instability in the ascending aerostat system. At the same time, we note that the positive definiteness of $\mathbf{K}$ is a necessary but not sufficient condition for stability ([28] pp. 36–40). We will see in the next section that, in spite of $\mathbf{K}$ being positive definite, flutter instability may set in the descending aerostat system. Here, we note from the Appendix that

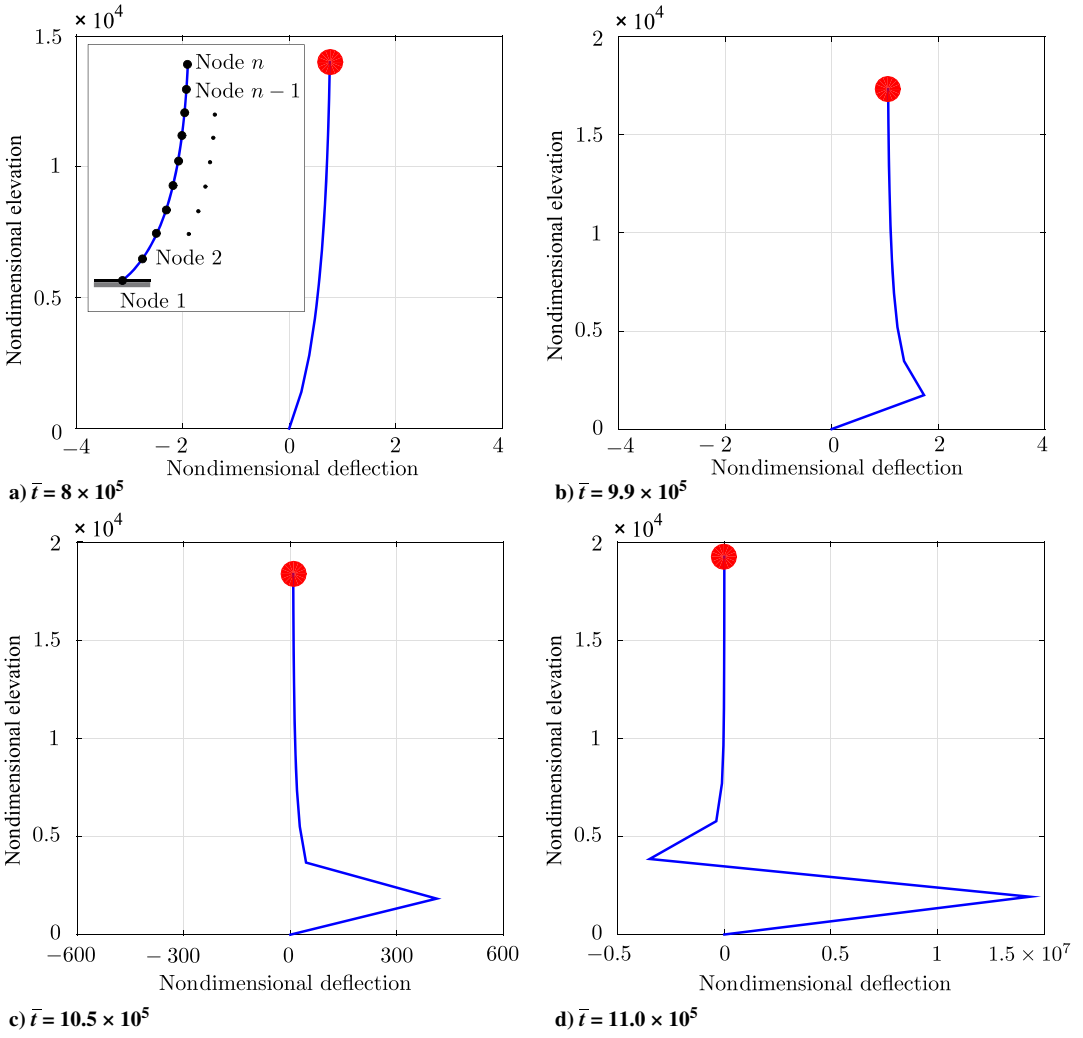

Fig. 6 Deflected shapes of the cable at different time instants while ascending at a constant rate of $\tilde{v} = 0.0175$.

$\det(\mathbf{G}) < 0$, which results in $g < 0$ for a descending aerostat system. We now compare our remarks for λ_i with computations.

We plot the evolution of the first three eigenvalues of Eq. (26) with $\bar{t}$ for different but constant rates of ascent in Fig. 9. Here, we observe that divergence instability sets in when $\lambda_1 = 0$ at $\bar{t} = \bar{t}^*$, which is defined in Fig. 7. Thus, the critical time $\bar{t} = \bar{t}^*$ found in Fig. 7 indeed defines the stability boundary for ascending aerostat systems for a given $\tilde{v}$. Hence, the motion, observed in Figs. 6a–6d, is due to divergence instability, which is now explained by employing a linear stability analysis.

The preceding analysis motivates us to develop deployment charts for ascending aerostats. Figure 10a shows stable and unstable operational regimes. This boundary separating two regimes is obtained by noting the time t^* at which the cable ascending at $\bar{v}_t$ first becomes unstable. Conversely, $\bar{v}_t$ is the minimum rate of ascent at which instability will initiate at t^*. Similarly, at a particular rate of ascent (say, $\tilde{v}_d$) we may find the critical time $\bar{t}_d^*$ beyond which the ascending aerostat is unstable.

Figure 10b shows another deployment chart for the critical elevation h_d^* that may be achieved in a stable manner at a given constant rate of ascent $\tilde{v}_d$. Figure 10b shows that, to achieve maximum elevation, the deployment of the aerostat should be done quasi statically, i.e., with $|\tilde{v}_d| \ll 1$. However, this is not practical. A possible alternative is to select a finite $\tilde{v}_d$ and augment the buoyancy force F_b instead. As shown in Fig. 10b, the maximum allowable elevation of the aerostat is greater at higher values of the net upward pull $F = F_b - mg$; cf. Eq. (9a). The latter may be achieved by expanding the volume of the aerostat. If the rate of deployment and the desired elevation is given, we may select an optimal F from Fig. 10b. We note from Fig. 10b that the overall maximum elevation achievable $h_{\max}$ is seen when the ascent rate is vanishingly small. The elevation $h_{\max}$ is regulated by the length of the cable at which the tension $P(0, t)$ at the bottom of the cable first becomes zero and, consequently, the aerostat system becomes unstable. At this time, the upward buoyancy force F_b balances the combined weight of the aerostat and the cable. This may be understood by noting that, when $P(0, t)$ vanishes, the resulting stiffness of the cable becomes zero locally, and hence $\mathbf{K}$ becomes singular. We emphasize that, at nonzero rates of deployment, that vanishing of the base tension is not the cause for the instability that regulates the maximum achievable elevation.

Finally, the rate of deployment of aerostats may not be kept constant during deployment. In Sec. VI, we investigate the case of nonconstant deployment rates.

V. Instability in Descending Aerostats

It was shown in Figs. 3b, 3d, 4b, and 4d that the first natural frequency of the oscillation and total energy of a descending aerostat system approach infinity as the cable's length $l \to 0$. We now investigate the stability of the aerostat system as it descends at a constant rate by considering the evolution of the eigenvalues of Eq. (26).

Consider first the structure of the matrices $\mathbf{M}$, $\mathbf{G}$, and $\mathbf{K}$ in Eq. (26), which is given in the Appendix. We observe that, for $\dot{l} < 0$, gyroscopic matrix $\mathbf{G}$ no longer remains positive definite. Thus, g becomes negative in Eq. (27), resulting in a positive real part in the eigenvalues λ_i, i.e., the λ_i always have a $\alpha_i > 0$ with $\beta_i \neq 0$. This,

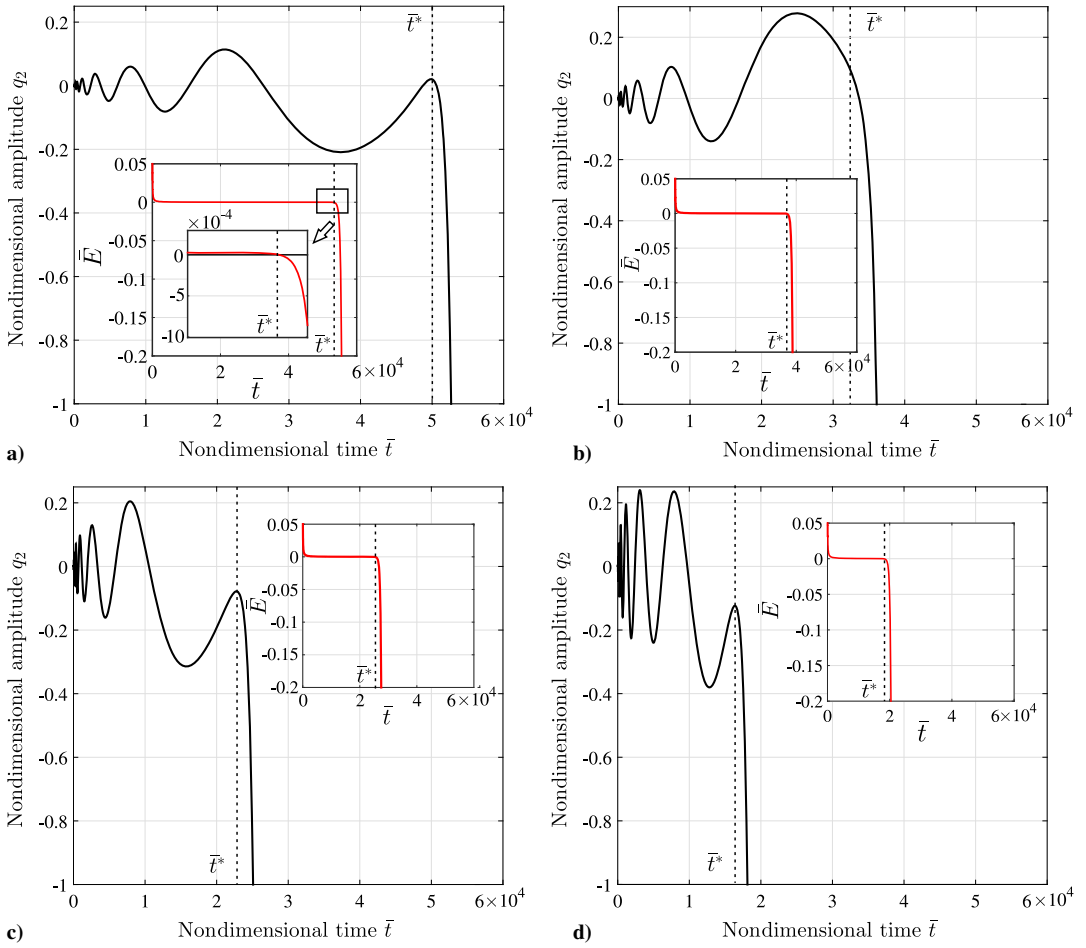

Fig. 7 Evolutions of deflection of node 2 and total nondimensional energy $\bar{E}$ (inset) in time for different rates of ascent: a) $\tilde{v} = 0.2$, b) $\tilde{v} = 0.3$, c) $\tilde{v} = 0.4$, and d) $\tilde{v} = 0.5$.

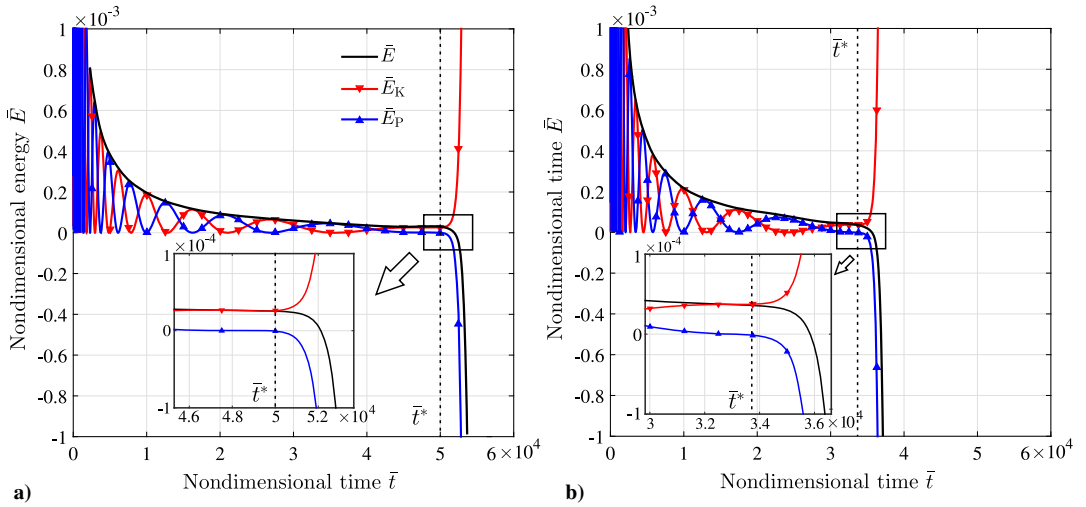

Fig. 8 Evolutions of total nondimensional energy $\bar{E}$, kinetic energy $\bar{E}_K$ and potential energy $\bar{E}_P$ with time for different rates of ascending: a) $\tilde{v} = 0.2$ and b) $\tilde{v} = 0.3$.

in turn, introduces flutter instability in the system [27]. This observation is confirmed by the evolution in Fig. 11 of λ_1, λ_2, and λ_3 found from FE computations. Figure 11 shows that λ_i $(i = 1, 2, 3)$ always have $\alpha_i > 0$ and $\beta_i \neq 0$. The magnitude of α_i initially remains very small. However, as $l \to 0$, α_2 and α_3 grow to infinity. This is because $\det(\mathbf{M}) \to 0$ as $l \to 0$ so that $\mathbf{M}$ eventually becomes singular at $l = 0$. Interestingly, α_1 0 for all $l(t)$ because of the presence of a heavy, lumped mass (the aerostat) at the end of the cable, which causes $\alpha_1 \ll \alpha_2, \alpha_3$; see the supplementary material for details. Figures 11a and 11b also show that the β_i increase with lowering l and, eventually, grow to infinity as $l \to 0$ and M becomes singular. The increase in β_i is in agreement with the asymptotic analysis of Fig. 2b, in which we se high-frequency oscillations as $l \to 0$. Physically, we may interpret a cable of $l \ll 1$ as a system with very high stiffness; indeed, we note from the Appendix that every element of $\mathbf{K} \propto 1/l$. Thus, analogous to a single-degree-of-freedom system, the aerostat system with high stiffness will have large natural frequencies, which are proportional to the eigenvalues of $\sqrt{\mathbf{M}^{-1}\mathbf{K}}$.

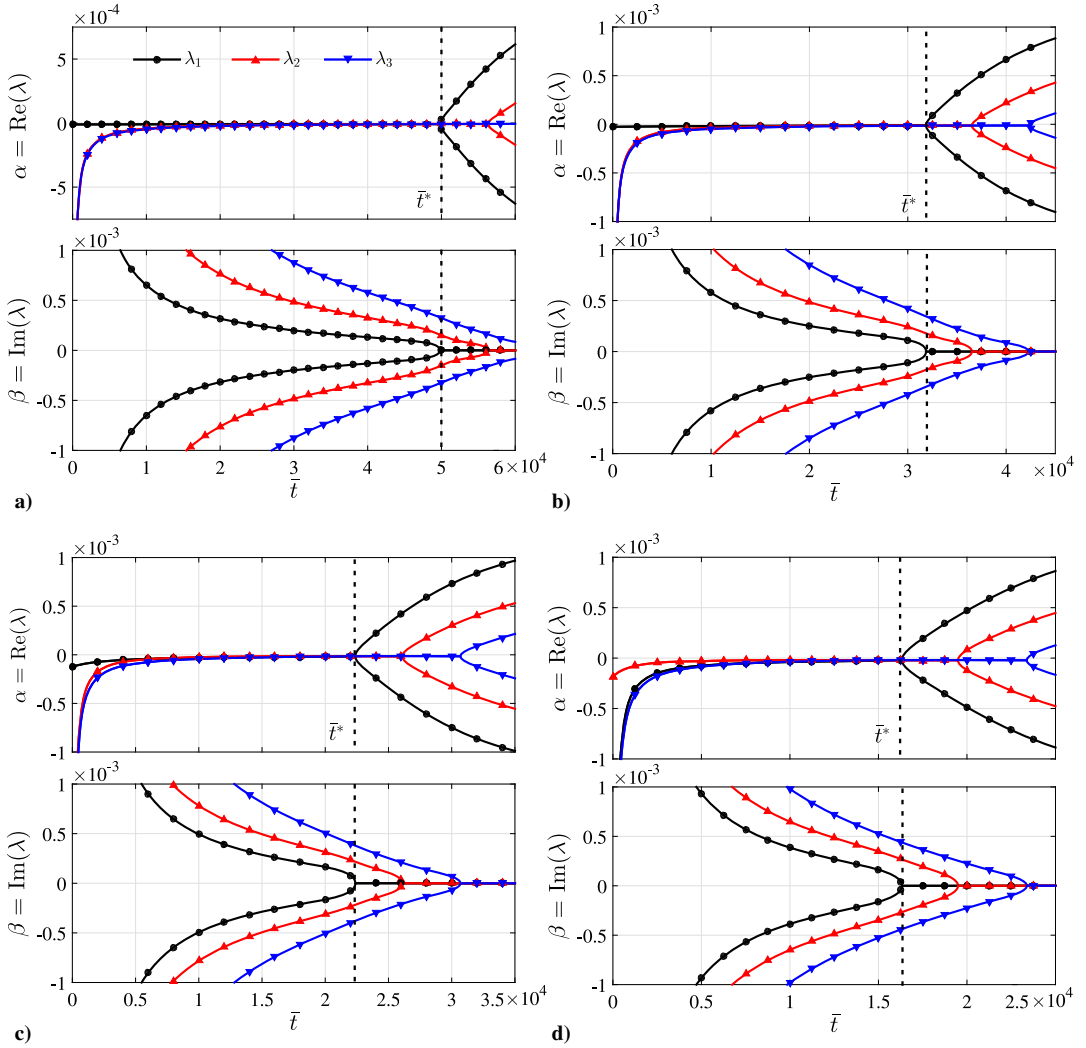

Fig. 9 Variation of real and imaginary parts of eigenvalues of first three modes shown for different rates of ascent: a) $\tilde{v} = 0.2$, b) $\tilde{v} = 0.3$, c) $\tilde{v} = 0.4$, and d) $\tilde{v} = 0.5$.

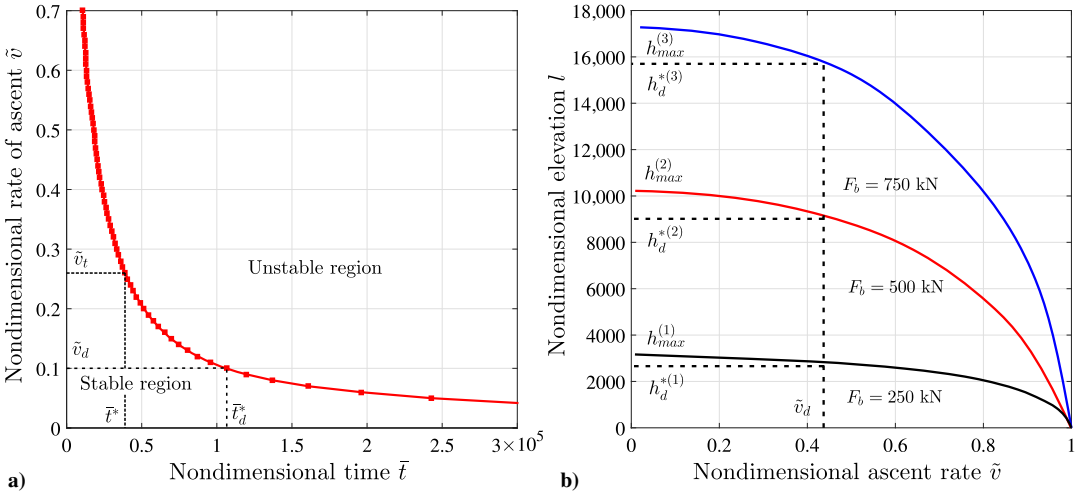

Fig. 10 Deployment charts: a) stability regime in $\bar{t}$–$\tilde{v}$ space, and b) maximum achievable elevation when the cable extends at a constant rate.

Figures 2b and 11a do not agree completely: Fig. 11 shows flutter instability sets in a descending aerostat and the fluttering frequency and amplitude increase as $l \to 0$. However, as $l \to 0$, in spite of an increase in the frequency, we see a temporal decay of the amplitude in Fig. 2b. To explain this disagreement, we divide the lateral end displacement q_{end} plotted in Fig. 2b by the changing length of the cable and plot $q_{\text{end}}/l(\bar{t})$ in Fig. 12 for two constant rates of descent. This scaling is required to represent the descending aerostat system by an equivalent system of constant length $l = 1$, which is necessary in order to compare with the computational stability analysis that is carried out at any time $\bar{t}$ only after fixing the cable's length at that time. This scaling should not be confused with the mapping of x onto

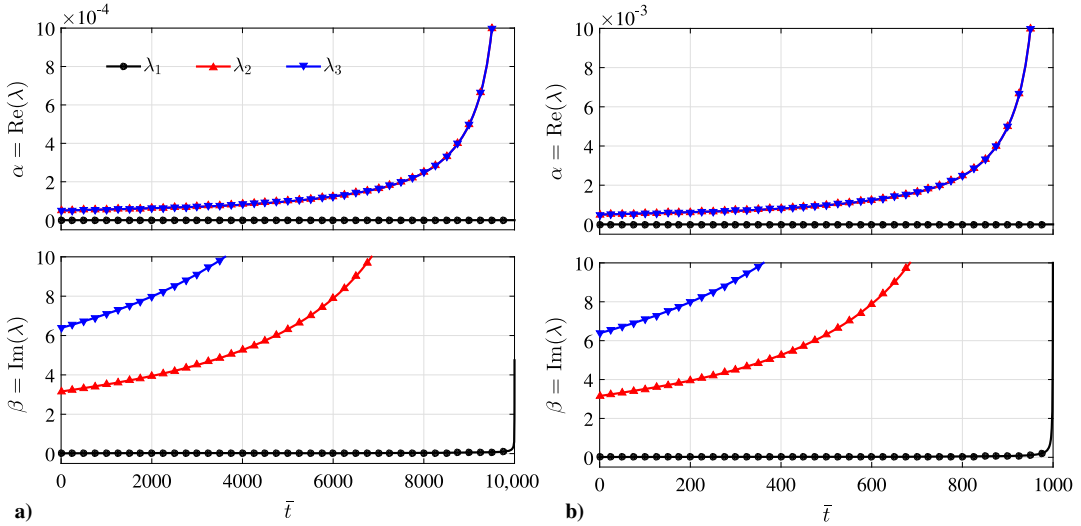

Fig. 11 Variation of real and imaginary parts of the eigenvalues of the first three modes, shown for two different rates of descent: a) $\tilde{v} = -0.0001$ and b) $\tilde{v} = -0.001$.

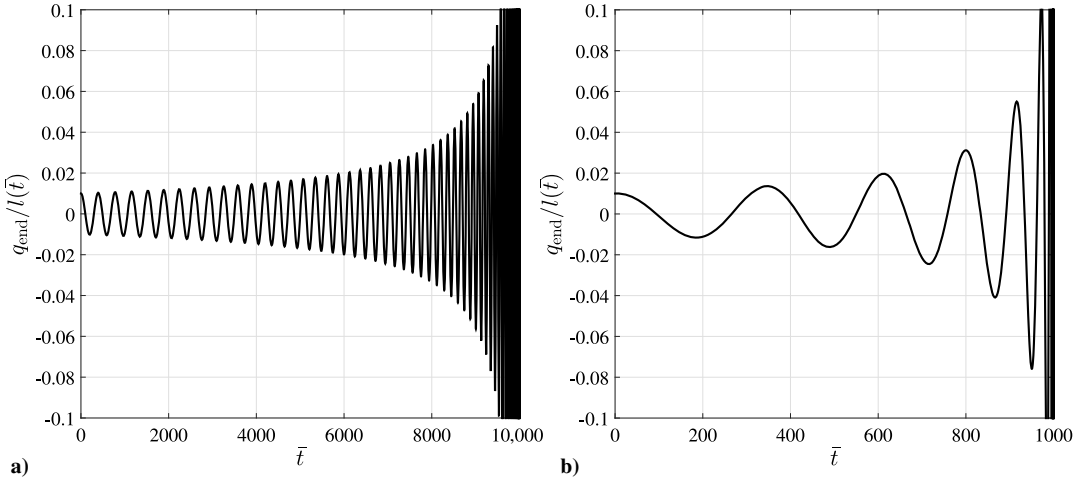

Fig. 12 Temporal evolution of the perturbed motion of the aerostat relative to its changing length for two constant descending rates: a) $\tilde{v} = -0.0001$ and b) $\tilde{v} = -0.001$.

ζ in Sec. II, which was introduced to map the aerostat system with changing lengths onto a unit length. The lateral displacement $y(x, t)$, however, was scaled by the initial length L_0 in Sec. II. Once we scale q_2 of Fig. 2b by $l(\bar{t})$, we do observe a flutter instability in the descending aerostat in Fig. 12, which confirms the predictions in Fig. 11, which were made on the basis of the system's eigenvalues.

Finally, increasing flutter as $l \to 0$ is similar to what is observed in shortening pendulums [44–46], in which the amplitude of oscillations blows up as $l \to 0$, and consequently the small amplitude assumption ceases to hold. Instability in shortening cables was explained on the basis of the temporal evolution of total energy by Zhu and Ni [18]. In contrast, we have followed a spectral analysis ([42] pp. 28–33) that, as discussed at the end of Sec. II, is the correct way to investigate instability in non-Hamiltonian gyroscopic systems (Yang and Mote [27] and Ziegler [28] pp. 36–40). From a practical standpoint, to avoid fluttering, the tether of the aerostat must have a finite length even when it is retracted to its lowest position. Moreover, retraction must be done with intermediate breaks; during which, the perturbations of the cable can be damped out by viscous air drag.

We now move on to investigate the effect of air flow on the dynamics of the cable.

VI. Forced Vibration

So far, we have not incorporated external forces (e.g., from air drag) into our analysis. We now investigate the forced response of the system. We begin by introducing a model for aerodynamic forces.

A. Aerodynamic Forces

Consider a lengthening/shortening cable that is attached to an aerostat, which is modeled as a rigid sphere. For simplicity, we consider air drag only on the aerostat and not on the cable. This is acceptable as a first approximation because we expect the drag on the cable to be much smaller as compared to that on the aerostat. A model for the dynamics of a rigid sphere (aerostat) submerged completely in a Newtonian fluid (air) is as follows [29–31]:

$$m\frac{\mathrm{d}V_i}{\mathrm{d}t} = m_f\left[\frac{\mathrm{D}u_i}{\mathrm{D}t} - \nu\Delta u_i\right]_{Y(t)} - \frac{1}{2}m_f\frac{\mathrm{d}}{\mathrm{d}t}[V_i(t) - u_i(\mathbf{Y}(t), t)] - 6\pi r\mu[V_i(t) - u_i(\mathbf{Y}(t), t)] + (m - m_f)g_i + F_i^{(e)} \tag{28}$$

where the operator $\mathrm{D}(\cdot)/\mathrm{D}t$ is defined as

$$\frac{\mathrm{D}(\cdot)_i}{\mathrm{D}t} = \frac{\partial(\cdot)_i}{\partial t} + \frac{\partial(\cdot)_i}{\partial x_j}(\cdot)_j$$

and the subscripts i and j represent different components of a vector; Δ is the Laplacian operator; m_f is the mass of air displaced by the aerostat; ν and μ are kinematic and dynamic viscosities of air, respectively; r is the radius of the aerostat with its center located at a position $\mathbf{Y}(t)$ and moving at a velocity $\mathbf{V}$; and $\mathbf{u}$ is the velocity of air. The term $m_f[\mathrm{D}u_i/\mathrm{D}t - \nu\Delta u_i]$ on the right-hand side of Eq. (28) is due to the pressure gradient imposed by the air flow. The second term

$$0.5m_f \mathrm{d}[V_i(t) - u_i(Y(t), t)]/\mathrm{d}t$$

is the added mass on the aerostat. The next three terms represent, respectively, the viscous Stokes drag, buoyancy, and (nonaerodynamic) external force $\mathbf{F}^{(e)}$ due to, in our case, the cable.

We consider only horizontal air flow for which the speed may vary vertically and with time. As μ_{air} is about 10^{-5} kg/(m$^{-1}\cdot$ s^{-1}), we take air to be inviscid. Because aerodynamic forces act only on the aerostat, the only change in the equations of motion will be in the boundary condition at $\zeta = 1$ [i.e., Eq. (10)] that, after nondimensionalizing (as in Sec. II), becomes

$$\tilde{m}\left[\eta_{,\bar{t}\bar{t}} + 2\frac{\dot{l}}{l}(1-\zeta)\eta_{,\zeta\bar{t}} + \frac{\dot{l}^2}{l^2}(1-\zeta)^2\eta_{,\zeta\zeta} - \zeta\frac{\ddot{l}}{l}\eta_{,\zeta}\right] + \frac{1}{l}\eta_{,\zeta} = \tilde{m}_f\left(\tilde{u}_{,\bar{t}} + \frac{\tilde{u}}{l}\tilde{u}_{,\zeta}\right) - \frac{1}{2}\tilde{m}_f\left[\eta_{,\bar{t}\bar{t}} + 2\frac{\dot{l}}{l}(1-\zeta)\eta_{,\zeta\bar{t}} + \frac{\dot{l}^2}{l^2}\{(1+\zeta^2)\eta_{,\zeta}\}_{,\zeta} + (1-\zeta)\frac{\ddot{l}}{l}\eta_{,\zeta} - \tilde{u}_{,\bar{t}}\right] \quad (29)$$

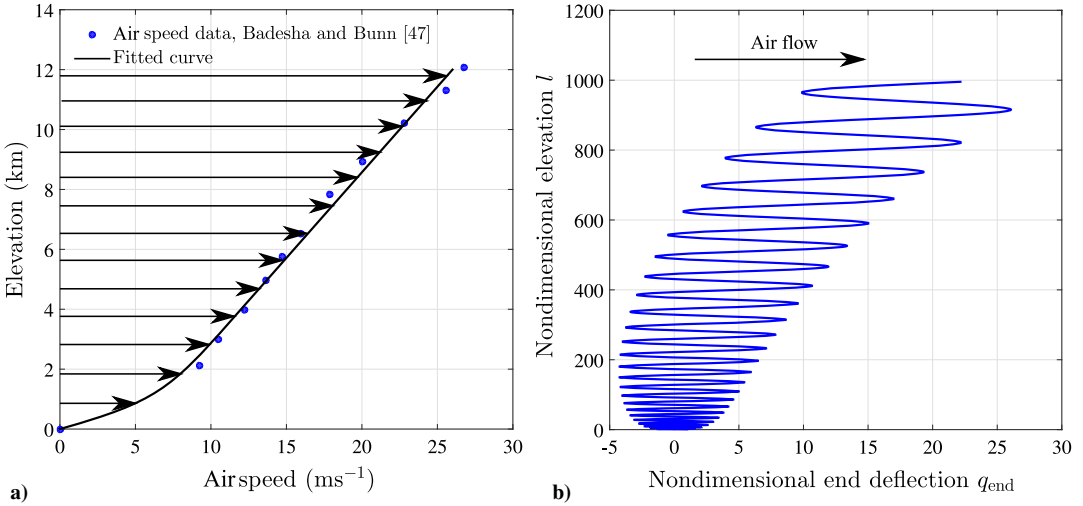

Fig. 13 Representations of a) steady velocity profile of air, and b) end-tip displacement of cable. The aerostat is ascending at a constant rate of $\tilde{v} = 0.0025$.

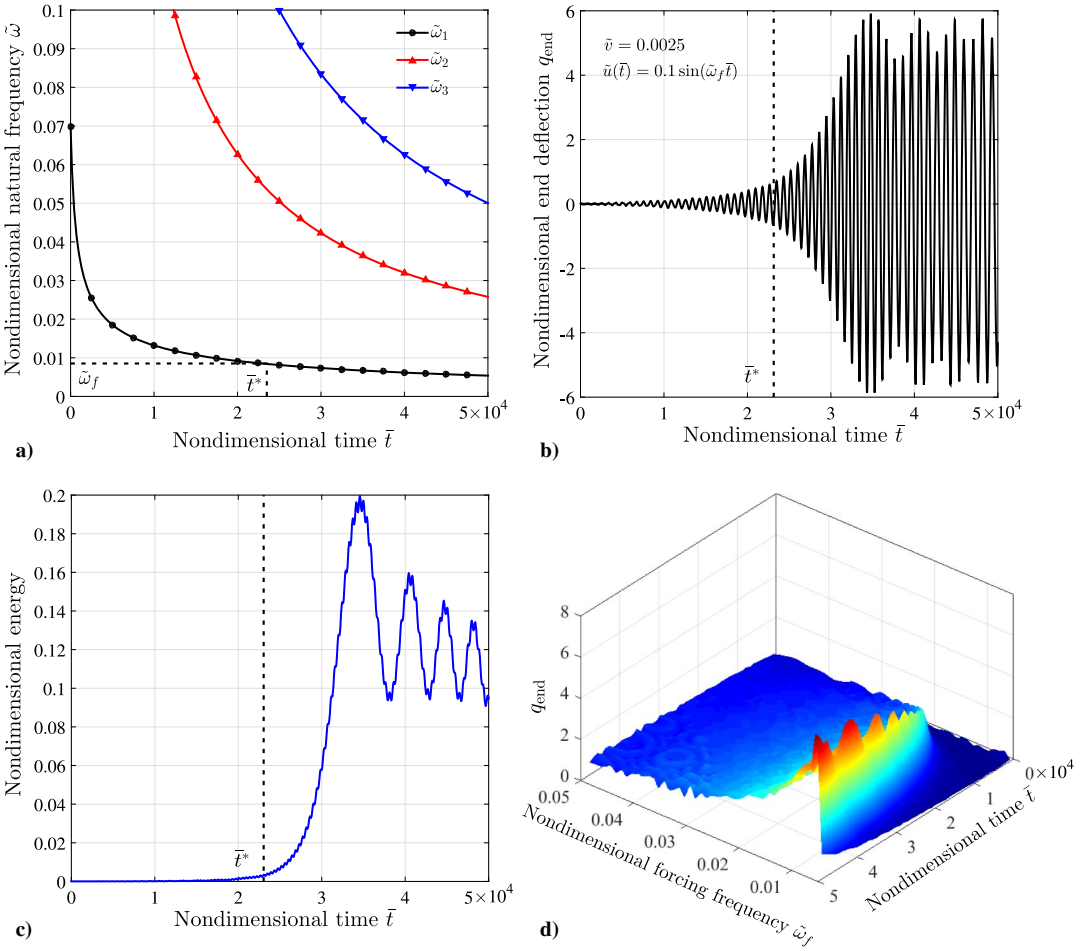

Fig. 14 Representations of a) variation of first three natural frequencies of the system with time, b) the time series response of end-tip displacement, c) variation of total energy, d) frequency domain response of the system.

where $\tilde{u}$ is the nondimensional velocity of air: $\tilde{u} = u\sqrt{\rho A/F}$, and $\tilde{m}_f = m_f/L_0\rho A$ is the nondimensional mass of the air displaced by the aerostat. In the preceding equation, we identified $\mathbf{V}$ and $Y(t)$ in Eq. (28) with, respectively, $\tilde{y}_{,tt}$ and $\zeta = 1$. We now investigate the effect of aerodynamic forces on the aerostat. Note that we ignore changes in the tension in the cable due to its lateral deflection. This is because of the very small inclination of the cable with the vertical (≈1.5 deg) as obtained from computations with practical aerostat data under wind load; see Fig. 13. The computation scheme is as discussed in the Appendix, but it now includes the modified boundary condition [Eq. (29)].

B. Results

In this section, we assume the density of air ($\rho_{\text{air}} = 1.205\ \text{kg/m}^{-3}$) remains constant with the altitude. We first consider a steady air flow profile, shown in Fig. 13a. The flow profile is obtained from the air flow data provided by Badesha and Bunn [47]. This air flow exerts drag on the aerostat. The temporal response for an ascending aerostat with a constant of $\tilde{v} = 0.0025$ is shown in Fig. 13b. The response is similar to that observed during free vibration, except that the mean of the oscillation shifts in the direction of air flow.

We now consider an air flow that is uniform in space but for which the amplitude changes with time as $\tilde{u}(\bar{t}) = 0.1\sin(\tilde{\omega}_f\bar{t})$. The cable extends at a constant rate of $\tilde{v} = 0.0025$. As the aerostat ascends, the natural frequencies of the system decrease. The temporal variations of the first three natural frequencies $\tilde{\omega}_1$, $\tilde{\omega}_2$, and $\tilde{\omega}_3$ of the system are depicted in Fig. 14a. We note from Fig. 14a that there will always be a time $\bar{t}^*$ after which one of the natural frequencies of the system will match $\tilde{\omega}_f$. As an example, we take $\tilde{\omega}_f = 0.0075$ and note the corresponding $\bar{t}^*$ from Fig. 14a at which $\tilde{\omega}_f$ equals $\tilde{\omega}_1$. As shown in Fig. 14b, the system resonates when $\bar{t} = \bar{t}^*$. Figure 14c confirms that there is a sudden change in the total energy of the system at $\bar{t} = \bar{t}^*$. However, the aerostat's displacement q_{end} cannot grow continuously because the natural frequency of the system shifts away from $\tilde{\omega}_f$ when time goes beyond $\bar{t}^*$. Finally, the frequency domain response of the system is shown in Fig. 14d. The surface shown in Fig. 14d is the envelope of q_{end} for various excitation frequencies $\tilde{\omega}_f$. We note that large-amplitude vibrations occur in the range of $0 < \tilde{\omega}_f < 0.03$. Our computations predict that, when $\tilde{\omega}_f \geq 0.03$, vibration amplitudes are not very large because they are driven by resonant interactions with the second or higher modes of the system. Figure 14d matches qualitatively with the experimental results of Yamamoto et al. [48], who investigated forced vibration of a lengthening/shortening cable that was fixed at its ends.

Next, we investigate the frequency domain response of a descending aerostat. The aerostat system is taken to be retracting at a constant rate of $\tilde{v} = 0.0025$. We note from Fig. 15a that the first natural frequency slowly grows from $\tilde{\omega}_1 = 0.08$. Therefore, we expect resonance when $\tilde{\omega}_f \geq 0.08$. We again define time $\bar{t}^*$ in Fig. 15a as the time at which $\tilde{\omega}_1 = \tilde{\omega}_f$. We set $\tilde{\omega}_f = 0.1$ and obtain the time domain response for end deflection and velocity; see Fig. 15b. We observe from Fig. 15b that the amplitude begins to grow at $\bar{t} = \bar{t}^*$. As before, the amplitude cannot grow continuously as the first natural frequency of the system shifts from $\tilde{\omega}_f$. The total energy of a shortening cable is seen to increase with time for reasons discussed in Sec. III. We find from Fig. 15c that energy now grows even more rapidly due to resonance. Finally, the frequency domain response of the system is depicted in Fig. 15d. We note that amplitudes do not grow for excitation frequencies beyond 0.3. It suggests that resonance in a shortening cable is significant only for $\tilde{\omega}_f$ near its first natural frequency $\tilde{\omega}_1$. Figure 15d is also in a good

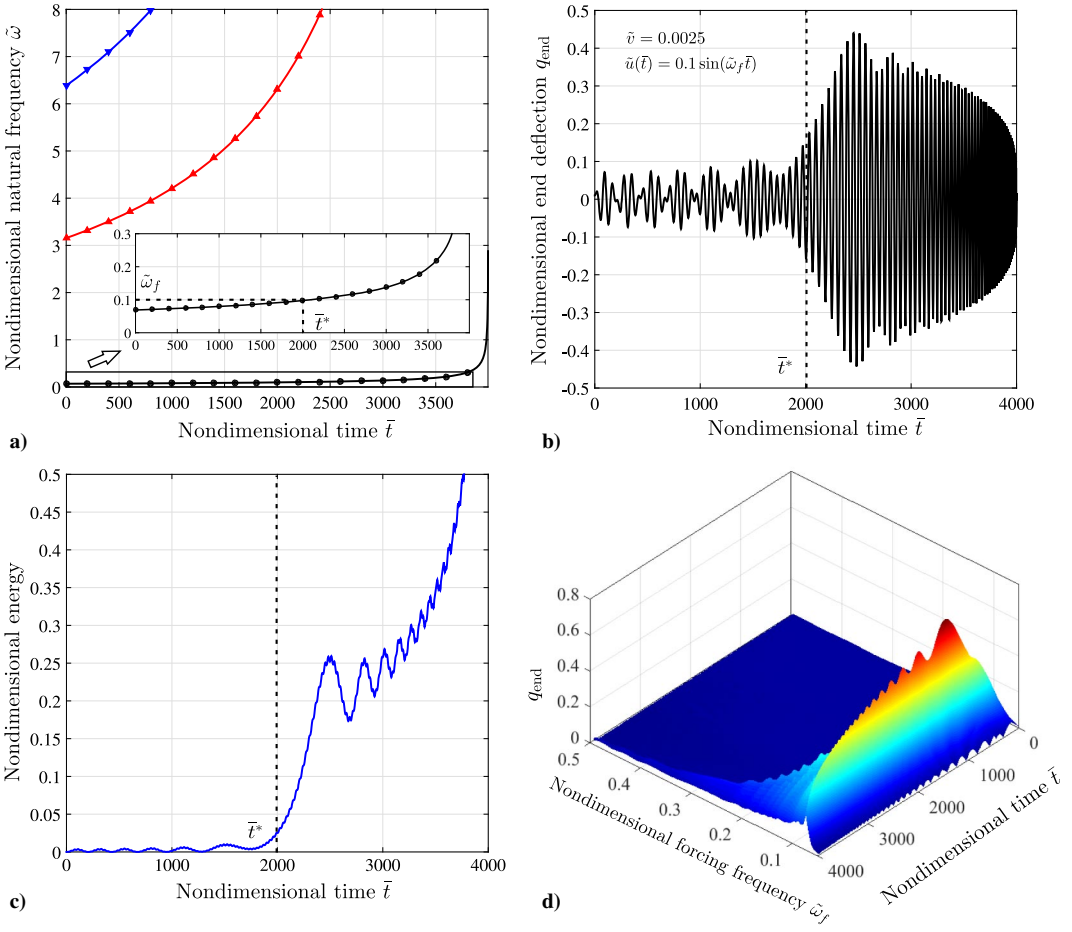

Fig. 15 Representations of a) variation of first three natural frequencies of the system in time, b) time series response of end-tip displacement, c) variation of total energy, and d) frequency domain response of the system.

qualitative match with the experimentally obtained frequency domain response of a shortening cable that has both of its ends fixed [48].

We end this section with two comments. The waviness in the energy plots of Figs. 14c and 15c is due to the periodicity in the aerodynamic forcing. The waviness in the surface plots Figs. 14d and 15d is due to the waviness in the envelope of the amplitudes, as extracted directly from the simulations. Waviness in the frequency domain response was also observed in the experiments on forced vibrations of lengthening/shortening cables by Yamamoto et al. [48].

VII. Case Studies

Finally, we demonstrate the practical applicability of our results through two studies of ascent of an aerostat from an initial tether length of $L_0 = 1$ m in the presence of air flow. We first note from Fig. 10b that, when there is no wind present, with $F_b = 500$ kN, an elevation of 10 km can be safely achieved at a constant rate of ascent $v = 1.2$ ms^{-1}, which corresponds to a nondimensional $\tilde{v} \approx 0.004$. A constant rate of ascent/descent of $v \approx 1.0$–1.2 ms^{-1} is typical for an aerostat system [37,38,47]. We now investigate the effect of the air flow profile shown in Fig. 16a, which is a fitted smooth curve to the air flow data obtained from Badesha and Bunn [47]. Furthermore, the rate of ascent v will now follow a prescribed temporal profile.

In the first case, the aerostat is set to ascend up to an elevation of 5 km, which is a typical elevation for an aerostat [8,41] and is less than the nominal safe elevation limit of 10 km. We plot the end deflection q_{end} in Fig. 16b, whereas the profile of the ascent rate of the aerostat is depicted in Fig. 16c, which shows sharp acceleration/deceleration at the start/end of ascent. We find that the aerostat oscillates about a shifted equilibrium while lengthening, behaving similarly to the case of Sec. V. When the ascent is stopped, the cable continues to oscillate about a new, shifted equilibrium, as shown in Fig. 16b. The stability of the system is confirmed by its eigenvalues shown in Fig. 16d, in which the real parts of the eigenvalues always remain negative or zero throughout the ascent. We see large negative real parts of the second and third eigenvalues near $t = 0$ in Fig. 16d that rapidly go to zero. The presence of these negative real parts in λ_2 and λ_3 indicates the fast decay of energies in the second and third eigenmodes initially.

In the second case study, we investigate the deployment of the same aerostat following an ascent profile, as in the previous case study, but now up to an elevation of 12 km, which is greater than the nominal safe elevation limit for $F_b = 500$ kN; see Fig. 10b. We achieve this elevation by following an ascent profile that is qualitatively similar to Fig. 16c but now has a constant rate of ascent $v = 1.2$ ms^{-1} up to $t = 10{,}000$ s; after which, v reduces to zero as in Fig. 16c. The air flow profile is taken to be the same as in Fig. 16a.

The time series of the end deflection (aerostat) is shown in Fig. 17a. We see that the aerostat oscillates about an equilibrium position, shifted by air flow, up to $t < 8250$ s. Then, there is a sudden change in the dynamics of the ascending cable, and its amplitude starts growing exponentially. This corresponds to the time t^* at which the eigenvalues of the system begin acquiring positive real parts; see Fig. 17b. We observe that the system destabilizes during its ascent, i.e., before the target elevation of 12 km is achieved. This matches the prediction of the deployment chart of Fig. 10b that suggests 10 km as the safe deployment limit when $F_b = 500$ kN. This confirms again the utility of developing such deployment charts.

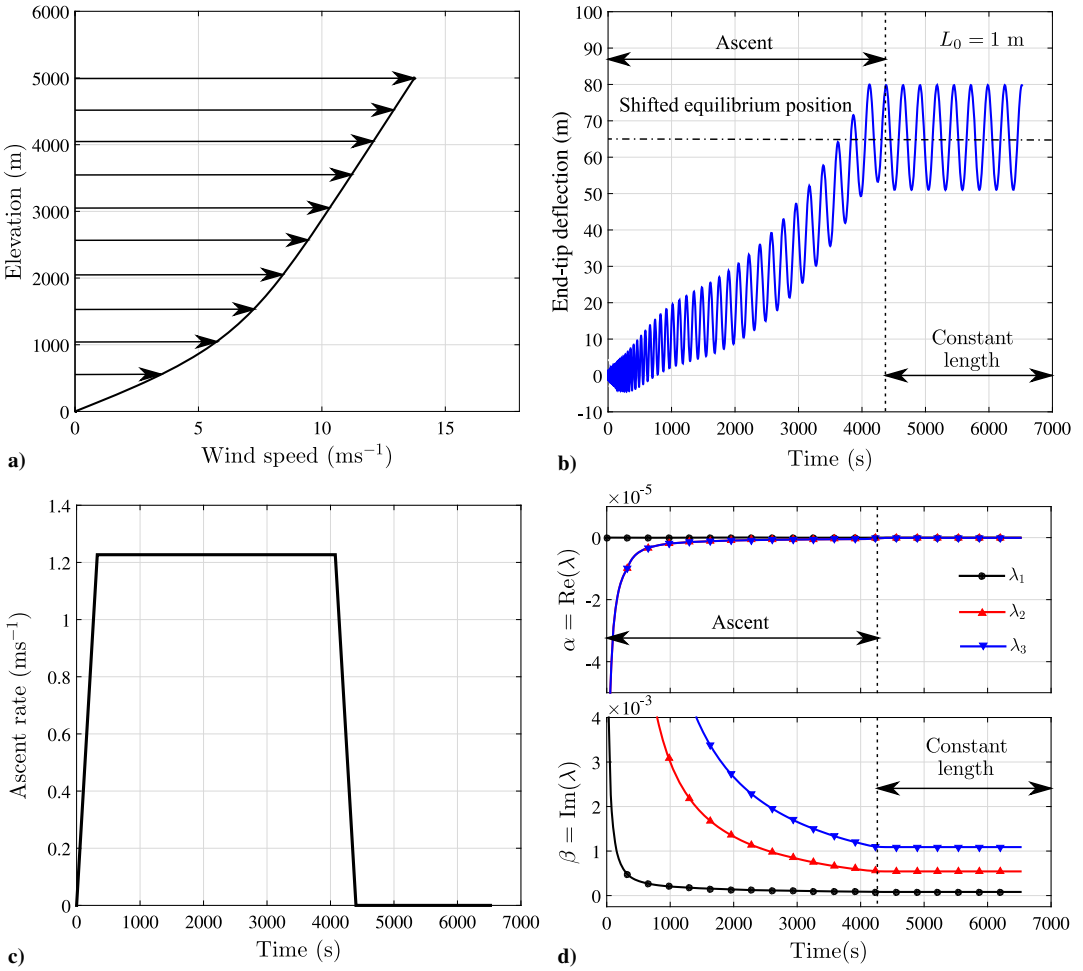

Fig. 16 Case study I: a) steady air flow profile, b) time series response for the end-tip displacement, c) temporal profile for the ascent rate, and d) evolution of first three eigenvalues in time.

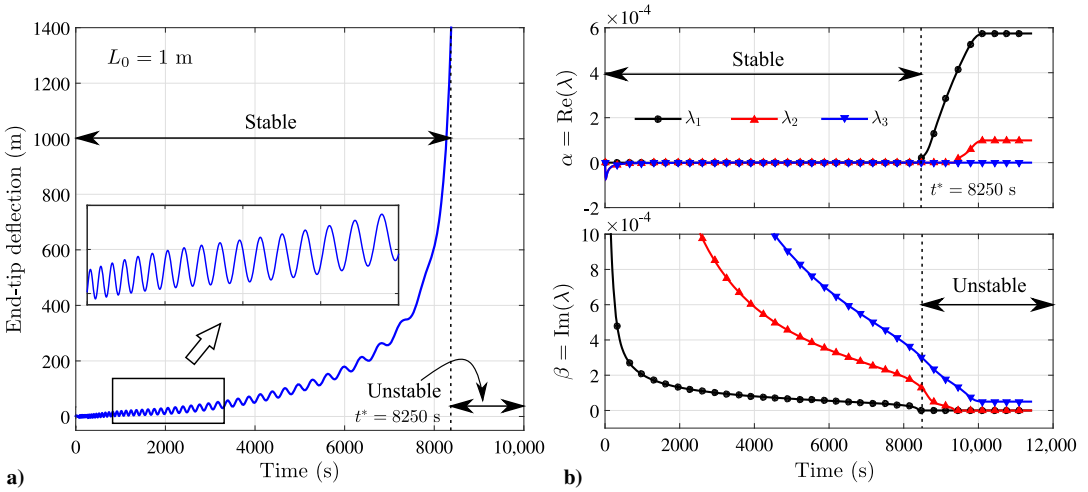

Fig. 17 Case study II: a) time series response for the end displacement, and b) evolution of first three eigenvalues in time.

VIII. Conclusions

In this paper, the dynamics of lengthening/shortening cables with end mass was investigated. First, an asymptotic analysis of the free vibrations of slowly ascending/descending aerostats was presented. The asymptotics matched well with the computationally obtained evolution of amplitude in time, and it matched qualitatively with the evolutions of the natural frequency and energy of the first eigenmode.

Then, in Sec. IV, the instability in ascending aerostats was investigated, and it was explained through a quasi-static eigenvalue analysis. Deployment charts based on this stability analysis were developed. These charts readily helped to estimate the maximum safely attainable elevation for a given rate of deployment. Instability in the descending aerostats was then investigated in Sec. V. The current quasi-static analysis successfully predicted flutter instability in descending aerostats, especially in the limit of $l \to 0$.

In Sec. VI, the forced vibration of ascending/descending aerostat systems in the presence of air flow through computations was investigated. The aerostat was modeled as a sphere and employed a simple model for the aerodynamic forces on the aerostat. The frequency domain response matched qualitatively with past experiments and underlined the tendency of strong resonance when the air frequency matched the evolving first natural frequency of the system at any point of time during ascent/descent.

Finally, the two case studies of aerostat systems concluded the paper, within which the stability analysis of previous sections was used. To make contact with practical scenarios, the aerostat to be deployed at nonconstant rates was considered. The current computed results were in good agreement with the limits obtained from deployment charts by considering the rate of deployment to be constant, as well as in the absence of air flow. This underlined the utility of developing deployment charts.

This work can be extended further for axially lengthening/shortening beams without much modification. A nonlinear elastic model for the cable can also be used. A small displacement assumption may not hold for highly flexible cables. Geometrically exact modeling of the heavy cable will help us to incorporate the large displacements and rotations. The current work and the proposed extensions will help create deployment charts predicated on a detailed stability analysis. These, in turn, will help develop predictive and optimized deployment strategies for aerostat systems.

Appendix: Finite Element Analysis

We solve Eq. (11) along with boundary conditions of Eq. (7) through the finite element method, for which the details are in the supplementary material. The main steps involve 1) expressing $\tilde{y}$ in terms of a spatial weighting function and a temporal component as $\tilde{y} = W(\xi)q(t)$, 2) forming the weighted residual and integrating by parts, and 3) following Galerkin's method for spatial discretization. In our FE analysis, we assume linear interpolating functions for a two-node cable element ij. Through this, we obtain the element mass, gyroscopic, and stiffness matrices for an element ij in index notation as $(\alpha, \beta = 1, 2)$

$$M_{\alpha\beta}^{(ij)} = l \int_{\zeta_i}^{\zeta_j} N_\alpha N_\beta \, \mathrm{d}\zeta \tag{A1}$$

$$G_{\alpha\beta}^{(ij)} = 2\dot{l} \int_{\zeta_i}^{\zeta_j} (1-\zeta) N'_\alpha N_\beta \, \mathrm{d}\zeta \tag{A2}$$

and

$$K_{\alpha\beta}^{(ij)} = \ddot{l} \int_{\zeta_i}^{\zeta_j} N'_\alpha N_\beta \, \mathrm{d}\zeta - \frac{\dot{l}^2}{l} \int_{\zeta_i}^{\zeta_j} (1-\zeta)^2 N'_\alpha N'_\beta \, \mathrm{d}\zeta + \int_{\zeta_i}^{\zeta_j} \left[\frac{1}{l} - \tilde{m}\frac{\ddot{l}}{l} - \left\{ \frac{1}{\tilde{F}} + \ddot{l} \right\} (1-\zeta) \right] N'_\alpha N'_\beta \, \mathrm{d}\zeta \tag{A3}$$

respectively, where

$$N_i = 1 - \frac{\zeta - \zeta_i}{h^e} \quad \text{and} \quad N_j = \frac{\zeta - \zeta_i}{h^e}$$

for all $\zeta_i \le \zeta \le \zeta_j$, and $N_i = N_j = 0$ otherwise. The preceding element matrices are then assembled to form the global mass $\mathbf{M}(\bar{t})$, gyroscopic $\mathbf{G}(\bar{t})$, and stiffness $\mathbf{K}(\bar{t})$ matrices, respectively. The boundary terms cancel each other at the time of assembly, except for the following contribution to $\mathbf{M}(\bar{t})$

$$\mathbf{M}(n,n) = \mathbf{M}(n,n) + \tilde{m} \tag{A4}$$

where n is the number of nodes, and h is the length of the last element of the cable, which is connected to the aerostat. Other boundary terms either vanish or get canceled at $\zeta = 1$. We finally obtain the spatially discretized form of Eq. (11) as

$$\mathbf{M}(\bar{t})\ddot{q}(\bar{t}) + \mathbf{G}(\bar{t})\dot{q}(\bar{t}) + \mathbf{K}(\bar{t})q(\bar{t}) = 0 \tag{A5}$$

The preceding equation is solved by an explicit Newmark time-marching algorithm to obtain temporal evolutions $q_i(t)$. Equation (A5) represents a polynomial eigenvalue problem, which governs the dynamics of the tethered aerostat system.

Acknowledgments

D. Mukherjee acknowledges the Ministry of Human Resources and Development, Government of India, for financial support during his M.Tech. program at Indian Institute of Technology (IIT) Kanpur

when this research was conducted. We are grateful to C. Venkatesan of Aerospace Engineering, IIT Kanpur, for encouraging us to take up this research and for insightful evaluations. We would like to thank Abhinav Dehadrai of Mechanical Engineering, IIT Kanpur, for helpful discussions. Finally, we would like to thank an anonymous referee for critical comments that greatly improved this work.

References

[1] Carrier, G. F., "The Spaghetti Problem," *American Mathematical Monthly*, Vol. 56, No. 10, 1949, pp. 669–672. doi:10.2307/2305560

[2] Mansfield, L., and Simmonds, J. G., "The Reverse Spaghetti Problem: Drooping Motion of an Elastica Issuing from a Horizontal Guide," *Journal of Applied Mechanics*, Vol. 54, No. 1, 1987, pp. 147–150. doi:10.1115/1.3172949

[3] Stylianou, M., and Tabarrok, B., "Finite Element Analysis of an Axially Moving Beam, Part I: Time Integration," *Journal of Sound and Vibration*, Vol. 178, No. 4, 1994, pp. 433–453. doi:10.1006/jsvi.1994.1497

[4] Stylianou, M., and Tabarrok, B., "Finite Element Analysis of an Axially Moving Beam, Part II: Stability Analysis," *Journal of Sound and Vibration*, Vol. 178, No. 4, 1994, pp. 455–481. doi:10.1006/jsvi.1994.1498

[5] Terumichi, Y., Ohtsuka, M., Yoshizawa, M., Fukawa, Y., and Tsujioka, Y., "Nonstationary Vibrations of a String with Time-Varying Length and a Mass-Spring Attached at the Lower End," *Nonlinear Dynamics*, Vol. 12, No. 1, 1997, pp. 39–55. doi:10.1023/A:1008224224462

[6] Gosselin, F., Paidoussis, M., and Misra, A., "Stability of a Deploying/Extruding Beam in Dense Fluid," *Journal of Sound and Vibration*, Vol. 299, No. 1, 2007, pp. 123–142. doi:10.1016/j.jsv.2006.06.050

[7] Kawaguti, K., Terumichi, Y., Takehara, S., Kaczmarczyk, S., and Sogabe, K., "The Study of the Tether Motion with Time-Varying Length Using the Absolute Nodal Coordinate Formulation with Multiple Nonlinear Time Scales," *Journal of System Design and Dynamics*, Vol. 1, No. 3, 2007, pp. 491–500. doi:10.1299/jsdd.1.491

[8] Aglietti, G., "Dynamic Response of a High-Altitude Tethered Balloon System," *Journal of Aircraft*, Vol. 46, No. 6, 2009, pp. 2032–2040. doi:10.2514/1.43332

[9] Jones, S., and Krausman, J., "Nonlinear Dynamic Simulation of a Tethered Aerostat," *Journal of Aircraft*, Vol. 19, No. 8, 1982, pp. 679–686. doi:10.2514/3.57449

[10] Lambert, C., and Nahon, M., "Stability Analysis of a Tethered Aerostat," *Journal of Aircraft*, Vol. 40, No. 4, 2003, pp. 705–715. doi:10.2514/2.3149

[11] Kang, W., and Lee, I., "Analysis of Tethered Aerostat Response under Atmospheric Turbulence Considering Nonlinear Cable Dynamics," *Journal of Aircraft*, Vol. 46, No. 1, 2009, pp. 343–348. doi:10.2514/1.38599

[12] Hembree, B., and Slegers, N., "Tethered Aerostat Modeling Using an Efficient Recursive Rigid-Body Dynamics Approach," *Journal of Aircraft*, Vol. 48, No. 2, 2011, pp. 623–632. doi:10.2514/1.C031179

[13] Mi, L., and Gottlieb, O., "Nonlinear Dynamics and Internal Resonances of a Planar Multi-Tethered Spherical Aerostat in Modulated Flow," *Meccanica*, Vol. 51, No. 11, 2016, pp. 2689–2712. doi:10.1007/s11012-016-0486-z

[14] Mankala, K. K., and Agrawal, S. K., "Dynamic Modeling and Simulation of Satellite Tethered Systems," *Journal of Vibration and Acoustics*, Vol. 127, No. 2, 2005, pp. 144–156. doi:10.1115/1.1891811

[15] Mankala, K. K., and Agrawal, S. K., "Dynamic Modeling of Satellite Tether Systems Using Newton's Laws and Hamilton's Principle," *Journal of Vibration and Acoustics*, Vol. 130, No. 1, 2008, Paper 014501. doi:10.1115/1.2776342

[16] Pesce, C. P., "The Application of Lagrange Equations to Mechanical Systems with Mass Explicitly Dependent on Position," *Journal of Applied Mechanics*, Vol. 70, No. 5, 2003, pp. 751–756. doi:10.1115/1.1601249

[17] Crellin, E. B., Janssens, F., Poelaert, D., Steiner, W., and Troger, H., "On Balance and Variational Formulations of the Equation of Motion of a Body Deploying Along a Cable," *Journal of Applied Mechanics*, Vol. 64, No. 2, 1997, pp. 369–374. doi:10.1115/1.2787316

[18] Zhu, W., and Ni, J., "Energetics and Stability of Translating Media with an Arbitrarily Varying Length," *Journal of Vibration and Acoustics*, Vol. 122, No. 3, 2000, pp. 295–304. doi:10.1115/1.1303003

[19] Vu-Quoc, L., and Li, S., "Dynamics of Sliding Geometrically-Exact Beams: Large Angle Maneuver and Parametric Resonance," *Computer Methods in Applied Mechanics and Engineering*, Vol. 120, No. 1, 1995, pp. 65–118. doi:10.1016/0045-7825(94)00051-N

[20] Chung, J., Han, C., and Yi, K., "Vibration of an Axially Moving String with Geometric Non-Linearity and Translating Acceleration," *Journal of Sound and Vibration*, Vol. 240, No. 4, 2001, pp. 733–746. doi:10.1006/jsvi.2000.3241

[21] Parker, R., "Supercritical Speed Stability of the Trivial Equilibrium of an Axially-Moving String on an Elastic Foundation," *Journal of Sound and Vibration*, Vol. 221, No. 2, 1999, pp. 205–219. doi:10.1006/jsvi.1998.1936

[22] Wickert, J., and Mote, C., "Classical Vibration Analysis of Axially Moving Continua," *Journal of Applied Mechanics*, Vol. 57, No. 3, 1990, pp. 738–744. doi:10.1115/1.2897085

[23] Elmaraghy, R., and Tabarrok, B., "On the Dynamic Stability of an Axially Oscillating Beam," *Journal of the Franklin Institute*, Vol. 300, No. 1, 1975, pp. 25–39. doi:10.1016/0016-0032(75)90185-4

[24] Zajaczkowski, J., and Lipiński, J., "Instability of the Motion of a Beam of Periodically Varying Length," *Journal of Sound and Vibration*, Vol. 63, No. 1, 1979, pp. 9–18. doi:10.1016/0022-460X(79)90373-0

[25] Hyun, S., and Yoo, H., "Dynamic Modelling and Stability Analysis of Axially Oscillating Cantilever Beams," *Journal of Sound and Vibration*, Vol. 228, No. 3, 1999, pp. 543–558. doi:10.1006/jsvi.1999.2427

[26] Nawrotzki, P., and Eller, C., "Numerical Stability Analysis in Structural Dynamics," *Computer Methods in Applied Mechanics and Engineering*, Vol. 189, No. 3, 2000, pp. 915–929. doi:10.1016/S0045-7825(99)00407-7

[27] Yang, S.-M., and Mote, C., "Stability of Non-Conservative Linear Discrete Gyroscopic Systems," *Journal of Sound and Vibration*, Vol. 147, No. 3, 1991, pp. 453–464. doi:10.1016/0022-460X(91)90493-4

[28] Ziegler, H., *Principles of Structural Stability*, Vol. 35, Birkhäuser Boston, Cambridge, MA, 2013, pp. 36–40. doi:10.1007/978-3-0348-5912-7

[29] Tchen, C.-M., "Mean Value and Correlation Problems Connected with the Motion of Small Particles Suspended in a Turbulent Fluid," Ph.D. Thesis, Delft Univ. of Technology, Delft, The Netherlands, 1947.

[30] Corrsin, S., and Lumley, J., "On the Equation of Motion for a Particle in Turbulent Fluid," *Applied Scientific Research*, Vol. 6, No. 2, 1956, pp. 114–116. doi:10.1007/BF03185030

[31] Maxey, M. R., and Riley, J. J., "Equation of Motion for a Small Rigid Sphere in a Nonuniform Flow," *Physics of Fluids*, Vol. 26, No. 4, 1983, pp. 883–889. doi:10.1063/1.864230

[32] Mukherjee, D., "Dynamics and Stability of Lengthening and Shortening Heavy Cables with End Mass," M.S. Thesis, Indian Inst. of Technology Kanpur, India, 2016.

[33] Miranker, W. L., "The Wave Equation in a Medium in Motion," *IBM Journal of Research and Development*, Vol. 4, No. 1, 1960, pp. 36–42. doi:10.1147/rd.41.0036

[34] Renshaw, A. A., Rahn, C. D., Wickert, J. A., and Mote, C. D., "Energy and Conserved Functionals for Axially Moving Materials," *Journal of Vibration and Acoustics*, Vol. 120, No. 2, 1998, p. 634. doi:10.1115/1.2893875

[35] Roy, A., and Chatterjee, A., "Vibrations of a Beam in Variable Contact with a Flat Surface," *Journal of Vibration and Acoustics*, Vol. 131, No. 4, 2009, Paper 041010. doi:10.1115/1.3086930

[36] Hagedorn, P., and Dasgupta, A., *Vibrations and Waves in Continuous Mechanical Systems*, Wiley, New York, 2007, pp. 47–49.

[37] Reed, H., and Sechrist, J., "Tethered Aerostats—Technology Improvements," *2nd Lighter Than Air Systems Technology Conference, Lighter-Than-Air Conferences*, AIAA Paper 1977-1184, 1977. doi:10.2514/6.1977-1184

[38] Badesha, S. S., Euler, A. J., and Schroeder, L., "Very High Altitude Tethered Balloon Trajectory Simulation," *AIAA Atmospheric Flight Mechanics Conference*, AIAA Paper 1996-3440, 1996. doi:10.2514/6.1996-3440

[39] Bender, C. M., and Orszag, S. A., *Advanced Mathematical Methods for Scientists and Engineers*, Springer Science and Business Media, New York, 1978, pp. 556–559. doi:10.1007/978-1-4757-3069-2

[40] Hinch, E. J., *Perturbation Methods*, Cambridge Univ. Press, New York, 1991, pp. 127–129.

[41] Aglietti, G., Markvart, T., Tatnall, A., and Walker, S., "Solar Power Generation Using High Altitude Platforms Feasibility and Viability," *Progress in Photovoltaics: Research and Applications*, Vol. 16, No. 4, 2008, pp. 349–359. doi:10.1002/pip.v16:4

[42] LaSalle, J. P., and Lefschetz, S., *Stability by Liapunov's Direct Method: With Applications*, Vol. 4, Academic Press, New York, 1961.

[43] Huseyin, K., Hagedorn, P., and Teschner, W., "On the Stability of Linear Conservative Gyroscopic Systems," *Zeitschrift für Angewandte Mathematik und Physik*, Vol. 34, No. 6, 1983, pp. 807–815. doi:10.1007/BF00949057

[44] Brearley, M. N., "The Simple Pendulum with Uniformly Changing String Length," *Proceedings of the Edinburgh Mathematical Society*, Vol. 15, No. 1, 1966, pp. 61–66. doi:10.1017/s0013091500013365

[45] Ross, D. K., "The Behaviour of a Simple Pendulum with Uniformly Shortening String Length," *International Journal of Non-Linear Mechanics*, Vol. 14, No. 3, 1979, pp. 175–182. doi:10.1016/0020-7462(79)90034-9

[46] Asadi-Zeydabadi, M., "Bessel Function and Damped Simple Harmonic Motion," *Journal of Applied Mathematics and Physics*, Vol. 2, No. 4, 2014, pp. 26–34. doi:10.4236/jamp.2014.24004

[47] Badesha, S. S., and Bunn, J. C., "Dynamic Simulation of High Altitude Tethered Balloon System Subject to Thunderstorm Windfield," *AIAA Atmospheric Flight Mechanics Conference*, AIAA Paper 2002-4614, 2002. doi:10.2514/6.2002-4614

[48] Yamamoto, T., Yasuda, K., and Kato, M., "Vibrations of a String with Time-Variable Length," *Bulletin of Japan Society of Mechanical Engineers*, Vol. 21, No. 162, 1978, pp. 1677–1684. doi:10.1299/jsme1958.21.1677